Ejection of the Massive Hydrogen-rich Envelope Timed with the Collapse of the Stripped SN 2014C

Raffaella Margutti[1], **A. Kamble**[2], **D. Milisavljevic**[2], **E. Zapartas**[3], **S. E. de Mink**[3], **M. Drout**[2], **R. Chornock**[4], **G. Risaliti**[5], **B. A. Zauderer**[6], **M. Bietenholz**[7,8], **M. Cantiello**[9], **S. Chakraborti**[2], **L. Chomiuk**[10], **W. Fong**[11], **B. Grefenstette**[12], **C. Guidorzi**[13], **R. Kirshner**[2], **J. T. Parrent**[2], **D. Patnaude**[2], **A. M. Soderberg**[2], **N. C. Gehrels**[14], and **F. Harrison**[15]

[1]Center for Interdisciplinary Exploration and Research in Astrophysics (CIERA), Department of Physics and Astronomy, Northwestern University, Evanston, IL 60208, USA [2]Harvard-Smithsonian Center for Astrophysics, 60 Garden Street, Cambridge, MA 02138, USA [3]Anton Pannenkoek Institute for Astronomy, University of Amsterdam, 1090 GE Amsterdam, The Netherlands [4]Astrophysical Institute, Department of Physics and Astronomy, 251B Clippinger Lab, Ohio University, Athens, OH 45701, USA [5]INAF-Arcetri Astrophysical Observatory, Largo E. Fermi 5, I-50125 Firenze, Italy [6]Center for Cosmology and Particle Physics, New York University, 4 Washington Place, New York, NY 10003, USA [7]Department of Physics and Astronomy, York University, Toronto, ON M3J 1P3, Canada [8]Hartebeesthoek Radio Observatory, P.O. Box 443, Krugersdorp 1740, South Africa [9]Kavli Institute for Theoretical Physics, University of California, Santa Barbara, CA 93106, USA [10]Department of Physics and Astronomy, Michigan State University, East Lansing, MI 48824, USA [11]Steward Observatory, University of Arizona, 933 North Cherry Avenue, Tucson, AZ 85721, USA [12]Cahill Center for Astrophysics, 1216 E. California Boulevard, California Institute of Technology, Pasadena, CA 91125, USA [13]University of Ferrara, Department of Physics and Earth Sciences, via Saragat 1, I-44122 Ferrara, Italy [14]NASA Goddard Space Flight Center, Code 661, Greenbelt, MD 20771, USA [15]Space Radiation Laboratory, California Institute of Technology, 1200 E California Boulevard, MC 249-17, Pasadena, CA 91125, USA

Abstract

We present multi-wavelength observations of SN 2014C during the first 500 days. These observations represent the first solid detection of a young extragalactic stripped-envelope SN out to high-energy X-rays ~40 keV. SN 2014C shows ordinary explosion parameters (E_k ~ 1.8×10^{51} erg and M_{ej} ~ 1.7 $M_\odot$). However, over an ~1 year timescale, SN 2014C evolved from an ordinary hydrogen-poor supernova into a strongly interacting, hydrogen-rich supernova, violating the traditional classification scheme of type-I versus type-II SNe. Signatures of the SN shock interaction with a dense medium are observed across the spectrum, from radio to hard X-rays, and revealed the presence of a massive shell of ~1 $M_\odot$ of hydrogen-rich material at ~6×10^{16} cm. The shell was ejected by the progenitor star in the decades to centuries before collapse. This result challenges current theories of massive star evolution, as it requires a physical mechanism responsible for the ejection of the deepest hydrogen layer of H-poor SN progenitors synchronized

with the onset of stellar collapse. Theoretical investigations point at binary interactions and/or instabilities during the last nuclear burning stages as potential triggers of the highly time-dependent mass loss. We constrain these scenarios utilizing the sample of 183 SNe Ib/c with public radio observations. Our analysis identifies SN 2014C-like signatures in ~10% of SNe. This fraction is reasonably consistent with the expectation from the theory of recent envelope ejection due to binary evolution if the ejected material can survive in the close environment for 10^3–10^4 years. Alternatively, nuclear burning instabilities extending to core C-burning might play a critical role.

Keywords

supernovae: individual (SN 2014C)

1. Introduction

Mass loss from massive stars (>10 $M_\odot$) plays a major role in the chemical enrichment of the Universe and directly determines the luminosity, life time, and fate of stars. However, the dominant channels and the physical mechanisms that drive mass loss in evolved massive stars are uncertain (see Smith 2014 for a recent review). This lack of understanding is significant because it further impacts our estimates of the stellar initial-mass function in galaxies and star formation through cosmic time, which rely on the predictions of stellar evolution models (Madau et al. 1998; Hopkins & Beacom 2006; Bastian et al. 2010).

Observations of stellar explosions across the electromagnetic spectrum obtained in recent years revealed that, contrary to theoretical expectations, massive stars often experience a complex history of mass-loss ejections before stellar death. These observations include the discovery of pre-explosion eruptions in >50% of H-rich massive stars, which are progenitors of ordinary Type-IIn SNe (Ofek et al. 2014), of which SN 2009ip is the best studied example (e.g., Fraser et al. 2013; Mauerhan et al. 2013a, 2014; Pastorello et al. 2013; Prieto et al. 2013; Margutti et al. 2014a; Smith 2014; Smith et al. 2014 and references therein), with SNe 2010mc (Ofek et al. 2013) and 2011ht (Roming et al. 2012; Mauerhan et al. 2013b; Fraser et al. 2013) being other examples. H-rich progenitors of super-luminous SNe-IIn can also experience episodic pre-SN mass loss, as was inferred for SN 2006gy (Smith et al. 2010a).

Interestingly, recent observational findings demonstrated that erratic mass-loss behavior preceding core-collapse extends to H-poor progenitors as well. A precursor to the SN explosion has been identified in the H-stripped type-Ibn SN 2006jc, which showed signs of interaction with a He-rich medium (e.g., Foley et al. 2007; Pastorello et al. 2007; Immler et al. 2008). Evidence for significantly enhanced mass loss timed with the explosion has been found for the H-poor progenitors of both type-IIb SNe (Gal-Yam et al. 2014; Kamble et al. 2015; Maeda et al. 2015) and type-Ib SNe (Svirski & Nakar 2014), as well as for the H-and He-poor progenitors of type-Ic SNe associated with some nearby gamma-ray bursts (Margutti et al. 2015; Nakar 2015). Along the same line, it is relevant to mention the possible detection of an outburst from the progenitor of the broad-line type-Ic SN PTF11qcj ~2.5 years before stellar death (Corsi et al. 2014), a possible precursor in the type-IIb SN

2012cs (Strotjohann et al. 2015), and the recent detection of interaction of the H-poor super-luminous SN iPTF13ehe with H-rich material at late times (Yan et al. 2015), as well the evidence for significant temporal variability in the radio light curves of Ib/c SNe (Soderberg 2007; Wellons et al. 2012), which suggests significant structure in their circumstellar media (CSM).

In all these SNe, the observations point to the presence of strongly time-dependent mass loss synchronized with core-collapse in a variety of stellar explosions (from type-IIn SNe to ordinary Ib/c, gamma-ray burst SNe and even super-luminous SNe). The erratic behavior of these stars approaching stellar death across the mass spectrum clearly deviates from the picture of steady mass loss through line-driven winds employed by current models of stellar evolution (e.g., Smith 2014). However, the nature of the physical process responsible for the highly time-dependent mass loss is at the moment a matter of debate. Equally unclear is the extent to which these processes have an active and important role in the evolutionary path that leads to the envelope-stripped progenitors of ordinary hydrogen-poor core-collapse SNe (i.e., SNe of type Ib/c).

We present multi-wavelength observations of the remarkable metamorphosis of SN 2014C, discovered by the Lick Observatory Supernova Search (Kim et al. 2014). SN 2014C evolved from an ordinary H-stripped core-collapse SN of type Ib into a strongly interacting type-IIn SN over ~1 year of observations. The relative proximity of SN 2014C in NGC 7331 ($d =$ 14.7 Mpc, Freedman et al. 2001) allowed us to witness the progressive emergence of observational signatures of the undergoing interaction across the electromagnetic spectrum, and, in particular, it offered us the unprecedented opportunity to follow the development of luminous X-ray emission captured in detail by the Swift X-ray Telescope (XRT), the *Chandra X-ray Observatory* (*CXO*), and the *Nuclear Spectroscopic Telescope Array* (*NuSTAR*). SN 2014C is the first young H-stripped SN for which we have been able to follow the evolution in the hard X-ray range. SN 2014C is also the first core-collapse envelope-stripped SN that showed a mid-InfraRed (midIR) rebrightening in the months after the explosion (Tinyanont et al. 2016).[16]

The paper is organized as follows. We describe observations of SN 2014C in Section 2, derive explosion properties in Section 3, derive environmental properties in Section 4, and discuss how SN 2014C compares to Ib/c SNe in Section 5. Based on these results, we discuss the challenges faced by the current theories of massive star evolution and explore alternatives in Section 6. We present our conclusions in Section 7. Details of the spectroscopic evolution of SN 2014C are provided in Milisavljevic et al. (2015; hereafter M15), while we refer to A. Kamble et al. (2017, in preparation; hereafter K17) for the modeling of the radio emission.

The time of first light is 2013 December 30 ±1 day (MJD 56656 ±1, see Section 3). Times will be referred to MJD 56656 unless explicitly noted. M15 estimate $E(B − V)_{tot}$ ~0.75 mag in the direction of the transient, which we will use to correct our photometry. The Galaxy

---

[16]A late-time midIR rebrightening attributed to shock interaction with the medium was detected for the type-Ia SN 2005gj (Fox & Filippenko 2013). It is relevant to mention here that a class of SNe Ia with late-time interaction with an H-rich medium has been recently identified (Silverman et al. 2013).

only contributes a limited fraction, corresponding to $E(B-V)_{mw}$ =0.08 mag (Cardelli et al. 1989; Schlafly & Finkbeiner 2011). Uncertainties are quoted at the level of 1σ confidence level unless stated otherwise.

2. Observations and Data Reduction

2.1. Optical–UV Photometry with Swift-UVOT

The UV-Optical Telescope (UVOT, Roming et al. 2005) on board *Swift* (Gehrels et al. 2004) started observing SN 2014C on 2014 January 6 (PIs P. Milne and R. Margutti). Due to its angular proximity to the Sun, SN 2014C was not observable by *Swift* in the time periods of late 2014 January–April and 2015 February–March. We employed the HEAsoft release v. 6.16 with the corresponding calibration files to reduce the data and a source extraction region of $3''$ to minimize the contamination from host-galaxy light. We extracted the photometry following the prescriptions by Brown et al. (2009).

SN 2014C is clearly detected in the wavelength range of 3500–5500 Å (i.e., UVOT *u*, *b*, and *v* filters) between −7 days and +7 days since maximum light (MJD 56663 $< t <$ MJD 56677; Figure 1). In the same time period, SN 2014C is only marginally detected in the UV (i.e., UVOT *w*1, *w*2 and *m*2 filters). SN 2014C reaches v-band maximum light around 2014 January 13 (MJD 56670). A search for increased UV emission arising from the SN shock interaction with the massive CSM in late-time ($t >$ 6 months) UVOT data led to a non-detection. Table 3 reports the complete UVOT photometry.

A comparison of the *v*-band light curve of SN 2014C to the SN Ib/c template by Drout et al. (2011) in Figure 2 illustrates that its rise time to maximum light of ~14 days falls on the short end of the observed distribution. The overall shape of the light curve is, however, in reasonable agreement with the template, which indicates a rather standard ejecta mass (M_{ej}) to kinetic energy (E_k) ratio, as quantified in Section 3.

2.2. Deep Late-time Optical Photometry with MMTCam

We obtained $r'i'$-band observations of SN 2014C with the MMTCam imager mounted on the 6.5 m MMT on 5 epochs spanning 2014 May 18–2015 May 23 (139–509 days since explosion, PI Margutti). All frames were bias, dark, and flat-field corrected using standard tasks in IRAF.[17] PSF photometry was performed on all images and absolute calibration was performed using five SDSS stars in a nearby standard field. The resulting photometry is listed in Table 4 and shown in Figure 10. No template subtraction was performed because the source was still visible in our final epoch of observation, and no sufficiently deep archival images were available in these bands. During our final epochs of observation, the source is ~0.6 mag brighter than the R-band pre-explosion source described in M15.

2.3. Early-time X-Ray Observations with Swift-XRT

The *Swift* X-Ray Telescope (XRT, Burrows et al. 2005) started observing SN 2014C on 2014 January 6th ($\delta t \sim$ 7 days since explosion, PI P. Milne). Observations acquired before

---

[17]IRAF is distributed by the National Optical Astronomy Observatory, which is operated by the Association for Research in Astronomy, Inc., under cooperative agreement with the National Science Foundation.

SN 2014C set behind the Sun cover the time interval of $t \sim 7$–20 days since the explosion (exposure of 17.2 ks). We detect significant X-ray emission at the SN site. However, inspection of pre-explosion images acquired in 2007 reveals the presence of diffuse X-ray emission that is not spatially resolved by the XRT. By accounting for the unresolved host-galaxy contribution, as constrained from pre-explosion observations, we infer a 3σ limit to the SN emission of 8.1×10^{-4} c s^{-1} (0.3–10 keV).

Coordinated observations of the *CXO* and *NuSTAR* obtained at later times (Sections 2.4 and 2.5) showed evidence for large intrinsic neutral hydrogen absorption in the direction of SN 2014C. At the time of the first *Chandra* observations we infer a total hydrogen column density $(3 \lesssim \mathrm{NH_{tot}} \lesssim 4) \times 10^{22}$ cm^{-2} (Sections 2.4, 2.6). The Galactic hydrogen column density is $\mathrm{NH_{mw}} \lesssim 6.1 \times 10^{20}$ cm^{-2} (Kalberla et al. 2005). The measured hydrogen column is thus dominated by material in the host galaxy of SN 2014C. Restricting our analysis to the 2–10 keV energy range to minimize the impact of the uncertain absorption of soft X-rays, and accounting for the unresolved host-galaxy contribution, we infer a 3σ limit to the SN emission of 3.0×10^{-4} c s^{-1} (2–10 keV). For $\mathrm{NH_{tot}} \sim 5 \times 10^{22}$ cm^{-2}, the corresponding unaborbed flux limit is $F_x < 4.1 \times 10^{-14}$ erg s^{-1} cm^{-2} and the luminosity limit is $L_x < 1.1 \times 10^{39}$ erg s^{-1} (2–10 keV). We assume a power-law spectral model with photon index $\Gamma = 2$, as appropriate for non-thermal Inverse Compton (IC) emission (see Section 4).

2.4. Deep X-Ray Observations with Chandra

Pre-Explosion—The field of SN 2014C was observed by the *CXO* on 2001 January 27th (PI Zezas, ID 2198). In 29.5 ks of observations, we find no evidence for X-ray emission at the SN site down to the limit of 2.6×10^{-4} c s^{-1} (0.3–10 keV). For an assumed power-law spectrum with photon index $\Gamma = 2$, the value above converts into an absorbed flux $<2.8 \times 10^{-15}$ erg s^{-1} cm^{-2} (0.3–10 keV), which corresponds to $L_x < 8.5 \times 10^{37}$ erg s^{-1} (0.3–10 keV).

Post-Explosion—We started a monitoring campaign with the *CXO* to constrain the evolution of SN 2014C on November 3, 2014 ($t = 308$ days, PI A. Soderberg, ID 16005). Other observations were acquired in 2015 under a multi-epoch program (PI R. Margutti, IDs 17569, 17570, 17571).

CXO data have been reduced with CIAO v4.6 and corresponding calibration files. Standard ACIS data filtering has been applied. SN 2014C is a bright source of X-ray emission with luminosity increasing with time (Figures 3 and 6). In our first epoch at $t = 308$ days, SN 2014C is detected at the level of $>40\sigma$, with a net count-rate of 0.013 c s^{-1} (0.5–8 keV, exposure time of 9.9 ks). A spectral fit with an absorbed power-law model $F_\nu \propto \nu^{-\beta}$ indicates very hard emission with $\beta = -1.5 \pm 0.3$. The detected X-ray emission is also in significant excess with respect to the extrapolation of the synchrotron spectrum that best fits the radio observations at all times (Figure 5). These two findings together suggest a thermal origin for the X-rays (as confirmed by coordinated *CXO–NuSTAR* observations obtained later). A fit with an absorbed bremsstrahlung model constrains $T > 10$ keV. We estimate the absorption at $t = 308$ days as follows. *Chandra* and *NuSTAR* observations obtained ~90 days later, at $t = 396$ days, are well modeled by a thermal bremsstrahlung spectrum with $T \sim 18$

keV (Section 2.6). The interaction of the SN shock with a very dense medium causes a rapid deceleration of the forward shock (FS) accompanied by a sudden and marked increase of the reverse shock (RS) temperature. At later times, the temperatures of the forward and RS decrease (see e.g., Chugai & Chevalier 2006, their Figure 2). SN 2014C started to interact with the dense shell ~100 days after the explosion (M15, i.e., ~200 days before the coordinated *CXO–NuSTAR* follow up, Section 4), which implies $T > 18$ keV at $t = 308$ days. Using this constraint to the temperature in our absorbed bremsstrahlung fit to the *CXO* data, we infer $NH_{tot} \lesssim 4 \times 10^{22}$ cm^{-2} at $t = 308$ days.

Ninety days later, ($t = 396$ days), our campaign reveals that SN 2014C substantially brightened with time, reaching 0.026 c s^{-1} in the 0.5–8 keV band ($> 90\sigma$ significance level detection using 9.9 ks of observations). From the spectral analysis, it is clear that the rebrightening is more apparent at soft X-ray energies ($E \lesssim 4$ keV), pointing to a decreased neutral hydrogen column density NH_{tot}. Our latest *CXO* observation was obtained at $t = 472$ days since explosion, with total exposure of 9.9 ks. SN 2014C is detected at the level of 0.0285 c s^{-1} ($> 100\sigma$ significance level, 0.5–8 keV). The spectral parameters at $t = 396$ days and $t = 472$ days are best constrained by the joint *CXO–NuSTAR* fit described in Section 2.6. The results from our broadband X-ray spectral fits and the resulting luminosities are reported in Table 1. Finally, in each of the three *CXO* observations, we note the presence of enhanced emission around 6.7–6.9 keV that we associate with H-like and He-like Fe line emission (Figure 4).

2.5. Hard X-Ray Observations with NuSTAR

We obtained two epochs of observations with the *NuSTAR* under approved DDT and Guest Investigator programs (PI Margutti), coordinated in time with the *CXO* at $t = 396$ days and $t = 472$ days since explosion. Our programs led to the first detection of a hydrogen-stripped core-collapse SN at hard X-ray energies. SN 2014C is well detected by *NuSTAR* in the energy range of 3–40 keV. The *NuSTAR* level 1 data products have been processed with the *NuSTAR* Data Analysis Software package version 1.4.1 included in the 6.16 HEASoft release. Event files were produced, calibrated, and cleaned using the standard filtering criteria and the latest files available in the *NuSTAR* calibration database (CALDB version 20150622). The total net exposures are 32.5 and 22.4 ks for the first and second observation, respectively. The source extraction radius is 1′ for both observations, and has been chosen in order to maximize the S/N. The background has been extracted in source-free regions in the the field of view. *NuSTAR* data are calibrated up to 79 keV; however, a comparison between the source and the background counts show that the spectrum is background-dominated above 30–40 keV. Therefore, we limited our spectral analysis to the range of 3–40 keV.

2.6. CXO–NuSTAR Spectral Modeling

The *CXO* covers the energy range of 0.3–10 keV, while *NuSTAR* is sensitive between 3 and 79 keV. The two instruments have very different point-spread functions (PSFs): while the *CXO* is able to spatially resolve the emission from SN 2014C from other sources in NGC7331 (Figure 3), the composite emission appears as a single source at higher energies due to the wider instrumental PSF of *NuSTAR* (FWHM of 18″). The emission from other

sources within the *NuSTAR* 1′ region is significantly fainter than SN 2014C. Nevertheless, to estimate and remove the contamination from other sources to the *NuSTAR* PSF, we employed the *CXO* observations as follows. For both epochs, we extracted a *CXO* spectrum of the contaminating sources by using an annular region with inner radius 1.5″ and outer radius of 1′ centered at the SN position. We model this spectrum with an absorbed power-law model to determine the best-fitting spectral parameters of the contaminating emission, and extrapolate its contribution to the *NuSTAR* energy band. We then add a spectral component with these parameters to the model used for the spectral fitting of the *NuSTAR* data, only. As a refinement of the method above, we extracted a spectrum of each point-like source that we detected with the *CXO* within the *NuSTAR* extraction region and fit the spectrum of each source with an absorbed power-law function that we extrapolate to the *NuSTAR* energy band, obtaining consistent results.

Accounting for the contaminating emission to the *NuSTAR* data as described above, we find that the two epochs of coordinated *CXO–NuSTAR* observations are well fit by an absorbed thermal bremsstrahlung spectral model with temperature $T \sim 20$ keV and decreasing absorption with time (Figure 4). We measure $NH_{tot} \sim 3 \times 10^{22}$ cm^{-2} and $NH_{tot} \sim 2 \times 10^{22}$ cm^{-2} at $t = 396$ days and $t = 472$ days, respectively. Table 1 reports the detailed results from the broadband X-ray spectral fitting while the resulting X-ray light curve of SN 2014C is portrayed in Figure 6.

Finally, we find evidence of an excess of emission around ~6.7–6.9 keV that we identify with H-and He-like transitions in Fe atoms. The Fe emission, as revealed by both the *CXO* and *NuSTAR*, is present in each of the three epochs of observations (Figures 4 and 5) with no detectable evolution from one epoch to the other. The results from a spectral line fitting with a Gaussian profile are reported in Table 2. Our observations do not have the spectral resolution and statistics to resolve what is likely to be a complex of emission lines originating from highly ionized Fe atom states, as suggested by the calculations by Mewe et al. (1985), Mewe et al. (1986) and Liedahl et al. (1995; e.g., the MEKAL model within Xspec).

3. Explosion Parameters

We calculate the bolometric luminosity by integrating the extinction-corrected flux densities in the *v*, *b*, and *u* UVOT bands and by applying a bolometric correction that corresponds to effective black-body temperatures in the range of 7000–10,000 K. We complement this data set with public photometry to constrain the very early light curve. Specifically, SN 2014C was first detected on 2014 January 2.10 UT. Kim et al. (2014) reports a detection of SN 2014C at the level of $R = 17.1$ mag. Assuming a bolometric correction appropriate for a temperature of emission $T \sim 10,000$–15,000 K, we derive $L_{bol} = (0.5$–$10) \times 10^{41}$ erg s^{-1} at $t \sim -10$ days since maximum light. Figure 7 shows the resulting bolometric emission from SN 2014C.

Before the onset of strong SN shock interaction at $t \sim 100$ days (M15), SN 2014C exhibited typical spectral features of type-Ib SNe (i.e., originating from stellar progenitors that managed to shed their hydrogen envelope, while retaining a helium layer). In the absence of

strong interaction, the light curves of H-poor SNe are powered by the radioactive decay of ^{56}Ni. Specifically, the optical peak luminosity directly reflects the amount of 56Ni produced by the explosion (M_{Ni}), while the light-curve width τ is sensitive to the photon diffusion timescale and thus to the explosion kinetic energy (E_k) and ejecta mass (M_{ej}). We employ the analytical model by Arnett (1982) with the updated formalism by Valenti et al. (2008) and Clocchiatti & Wheeler (1997) to estimate the explosion parameters of SN 2014C. We refer to Falk & Arnett (1977) for a detailed discussion of the effects of pre-SN mass loss on the observed light curves.

The spectra acquired around the time of maximum light indicate a photospheric velocity v_{phot} = 13,000 km s^{-1} (M15). We use v_{phot} as characteristic velocity v_* of the ejecta to break the degeneracy between M_{ej} and E_k, where[18] v_*=(10 E_k/3 M_{ej})$^{0.5}$ and assume a constant effective opacity k_{opt} = 0.07 cm^2 g^{-1}. Modeling of the bolometric light curve with the updated Arnett (1982) formalism described above constrains the time of first light of SN 2014C to 30 December 2013 ±1 day (MJD 56656 ±1) and yields the following estimates for the explosion parameters: M_{Ni} ~ 0.15 $M_{\odot}$, E_k ~ 1.8 × 10^{51} erg, M_{ej} ~ 1.7 $M_{\odot}$. The comparison to the sample of type Ib/c SNe in Figure 7 shows that the explosion parameters of SN 2014C are typical of the class of SNe with hydrogen-stripped progenitors (Drout et al. 2011; Cano 2013; Lyman et al. 2014).

As a caveat, we note that this analytic treatment is sensitive to $k_{opt}M_{ej}$ and $k_{opt}E_k$. As Wheeler et al. (2015) showed, a way to solve for this model degeneracy is by using the late-time light-curve decay slope under the assumption that it is entirely powered by the radioactive decay of ^{56}Ni and its products. This assumption does not hold for SN 2014C, which is dominated by interaction at late times (Figure 10). For ordinary Ib/c SNe, Wheeler et al. (2015) find k_{opt} values as low as 0.02 cm^2 g^{-1} (e.g., for SN 1994I, their Table 2). For SN 2014C, this low value of k_{opt} would imply E_k ~ 10^{52} erg. Energetic SNe with E_k ~ 10^{52} erg are accompanied by broad spectroscopic features that are not observed in SN 2014C (M15). We thus conclude that for SN 2014C it is likely that E_k < 10^{52} erg and the effective opacity is k_{opt} > 0.02 cm^2 g^{-1}. In the following, we use 30 December, 2013 as the explosion date of SN 2014C. The possible presence of a "dark phase" (e.g., Piro & Nakar 2013, 2014) with duration between hours and a few days between the explosion and the time of the first emitted light has no impact on our conclusions.

4. Environment

4.1. Low-density Cavity at R ≲ 2 × 10^{16} cm

At early epochs ($t \lesssim$ 30 days), the X-ray emission from SNe originating from H-stripped progenitors is dominated by Inverse Compton processes (e.g., Björnsson & Fransson 2004). Photospheric optical photons are upscattered to X-ray energies by relativistic electrons accelerated by the SN shock. IC emission depends on the density structure of the SN ejecta, the properties of the explosion, and the characteristics of the medium around the SN (e.g., Chevalier & Fransson 2006).

---

[18]We replaced the inaccurate numerical factor given in Equation (65) of Arnett (1982) with the correct value, as explained in Wheeler et al. (2015).

Following Matzner & McKee (1999), we assume an SN outer density structure $\rho_{SN} \propto R^{-n}$ with $n \sim 9$, as appropriate for stellar explosions arising from compact progenitors. The SN shock accelerates electrons into a power-law distribution $n_e(\gamma) \propto \gamma^{-p}$, where γ is the electron Lorentz factor. Well studied SNe Ib/c indicate $p \sim 3$, with a fraction of post-shock energy into electrons $e_e \sim 0.1$ (e.g., Chevalier & Fransson 2006). We use here the values of the explosion kinetic energy $E_k = 1.8 \times 10^{51}$ erg and ejecta mass $M_{ej} = 1.7\, M_\odot$ that we estimated in Section 3. Finally, the last stages of evolution of massive stars are predicted to be characterized by powerful winds, which are expected to shape the immediate SN environment within $R \sim 4 \times 10^{16}$ cm (e.g., Ramirez-Ruiz et al. 2001; Dwarkadas 2007) into a density profile $\rho_{CSM} \propto R^{-2}$.

By employing the IC formalism from Margutti et al. (2012) and the optical bolometric emission from SN 2014C of Section 3, we find that the lack of detectable X-ray emission from SN 2014C during the first ~20 days (Section 2.3) implies a low density environment at distances of $R \sim (0.8–2) \times 10^{16}$ cm. The inferred mass-loss rate is

$\dot{M} < (3 - 7) \times 10^{-6} M_\odot\, \mathrm{yr}^{-1}$ for an assumed wind velocity $v_w = 1000$ km s^{-1}. This result implies that the progenitor did not suffer massive eruptions within $t = 7(v_w/1000$ km s$^{-1})$ years before the final explosion.

4.2. Region of Dense H-rich Material at R ~ 5.5 × 10^{16} cm

The rising X-ray and radio luminosity, coupled with the progressive emergence of prominent Hα emission (Figure 10), suggests a scenario where the freely expanding, H-poor SN 2014C ejecta encountered a dense H-rich region in the proximity of the explosion site. We constrain the properties of the dense CSM shell by using the following observables.

1. Optical spectroscopy in M15 constrains the emergence of Hα emission due to the interaction of the SN ejecta with H-rich material in the CSM to $t > 30$ days. A prominent Hα profile has developed by day 130 after the explosion. In the following, we use $t = 130$ days as the start time of the strong CSM interaction.

2. The broadband X-ray luminosity shows a sharp rise during the first ~300 days and reaches its maximum value of $L_x \sim 5 \times 10^{40}$ erg s^{-1} by ~500 days.

3. The X-ray emission is of thermal origin and the observed temperature is $T \sim 20$ keV between 400 and 500 days after the explosion.

4. There is significant evidence for decreasing absorption with time, with NH_{tot} evolving from ~4×10^{22} cm^2 at ~300 days, to ~2×10^{22} cm^2 at ~500 days after the explosion.

The interaction of freely expanding SN ejecta with the CSM leads to the formation of a double shock interface layer, with the forward shock (FS) propagating into the CSM and the reverse shock (RS) decelerating the SN ejecta. We follow Chevalier (1982) to describe the dynamics of the shock propagation into the low-density bubble, and Chevalier & Liang (1989) to compute the dynamics of the strong interaction of the SN ejecta with the dense shell.

4.2.1. Expansion in the Bubble—The dynamics of the double shock structure that originates from the interaction of the outer power-law portion of the SN ejecta profile with a wind-like CSM with densit $\rho_{\mathrm{CSM}}=M/(4\pi v_w R^2)$ is described by a self-similar solution (Chevalier 1982). From Section 4.1, $M<(3-7)\times10^{-6} M_\odot\,\mathrm{yr}^{-1}$ for $v_W=1000$ km s^{-1}. With these parameters, we find that the FS radius at the time of the start of the strong interaction ($t=130$ days) is ~5.5×10^{16} cm. The swept up mass of gas within the bubble is $M_{\mathrm{bubble}}<10^{-4}\,M_\odot$. M_{bubble} is considerably smaller than the mass in the outer power-law section of the SN ejecta ($M_{\mathrm{ej,PL}}\sim0.6\,M_\odot$), which is thus only minimally decelerated during its expansion into the cavity. The velocity of the FS just before the start of the strong interaction is ~44,000 km s^{-1}. The CSM density at the outer edge of the bubble is <100 cm^{-3}.

4.2.2. Interaction with the Dense, H-rich CSM—The rising X-ray and radio luminosity with time is suggestive of a large density contrast between the bubble and the shell of CSM, as confirmed by our modeling below. Under these circumstances (i.e., $\rho_{\mathrm{bubble}}\ll\rho_{\mathrm{shell}}$ and $M_{\mathrm{ej,PL}}\gg M_{\mathrm{bubble}}$), the outer density profile of the SN ejecta continues to interact with the dense shell of CSM and the energy transmitted to the shell is initially modest (Chevalier & Liang 1989). The analysis by Chevalier & Liang (1989) shows that the flow once again has a self-similar nature, with $R_{\mathrm{RS}}=0.92\,R_{\mathrm{shell}}$ for $n=9$ (their Table 2).

The collision of the SN ejecta with the dense CSM shell causes a sudden increase of the X-ray luminosity of both the RS and the FS (see, e.g., Chugai & Chevalier 2006, their Figure 2). The FS experiences rapid deceleration, with v_{FS} decreasing from ~44,000 km s^{-1} to a ~ few 1000 km s^{-1}, as suggested by the measured width of the intermediate component of the Hα line in our spectra, which maps the dynamics of the shocked, H-rich CSM shell (Figure 10, M15). Since the velocity of the shock determines the energy imparted to particles that cross the shock, the characteristic temperature of emission of material in the FS plummets: contrary to the previous phase of expansion within the bubble, the interaction with a wall of material causes the FS temperature to be significantly below the temperature of the RS.

This rapid deceleration is followed by a period of steady acceleration as the faster SN ejecta piles up from behind (Chevalier & Liang 1989; Dwarkadas 2005). The radius of the shock wave expands as $R_{\mathrm{FS}}=R_{\mathrm{shell}}+K_1=\left(AR_{\mathrm{Shell}}^{2-n}t^{n-3}/\rho_{\mathrm{Shell}}\right)^{1/2}$, where $K_1=0.26$ for a nonradiative shock and $K_1=0.24$ for a radiative shock front, $n=9$, $A\equiv A(E_k, M_{\mathrm{ej}}, n)$ and we have assumed a smooth CSM shell with density ρ_{shell} (Chevalier 1984; Chevalier & Liang 1989).

We proceed within the "thin shell" approximation (e.g., Chevalier 1982), where the shocked gas, made by shocked CSM and shocked SN ejecta, can be treated as a thin shell with mass M_s, radius $R_s(t)$ and velocity $v_s(t)$. $v_{\mathrm{FS}}\approx v_s$, the velocity of the (unshocked) ejecta at the RS is $v_{\mathrm{SN}}=R_s/t$ and $v_{\mathrm{RS}}\approx v_{\mathrm{SN}}-v_{\mathrm{FS}}$. For a decelerated FS velocity $v_{\mathrm{FS}}\approx$ a few 1000 km s^{-1}, we estimate at $t\sim400$ days $R_s\sim6\times10^{16}$ cm and $v_{\mathrm{RS}}\sim13,000$ km s^{-1}. The RS temperature is directly connected to its velocity by $T_{\mathrm{RS}}=2.27\times10^9\mu_P v_{\mathrm{RS,4}}^2$ where $v_{\mathrm{RS,4}}\equiv v_{\mathrm{RS,4}}/10^4$ km s^{-1} and μ_p is the mean mass per particle including electrons and ions (e.g., Fransson et al. 1996). We follow Chugai & Chevalier (2006) and approximate the shocked SN ejecta by a

mixture of 65% He, 33% O, and 2% Fe by mass. For this composition of the ejecta and complete ionization, $\mu_p = 1.33$ and $T_{RS} > 400$ keV, which is much larger than the $T \sim 18$ keV indicated by our broadband X-ray spectral analysis (incomplete ionization would lead to even larger temperatures). This finding thus suggests that the detected X-ray emission is dominated by the FS. Under this hypothesis, $T_{FS} = 18$ keV at $t \sim 400$ days, which implies $v_{FS} \sim 4000$ km s^{-1}, consistent with the indication of $v_{FS} \sim$ few 1000 km s^{-1} from the optical spectra. Solar abundances have been assumed for the CSM (i.e., $\mu_p = 0.61$).

The mass of the shocked CSM material is directly constrained by the observed bremsstrahlung spectrum. The observed X-rays at $t \sim 500$ days, with $T \sim 20$ keV and $L_x \sim 5 \times 10^{40}$ erg s^{-1} require an emission measure $EM_{FS} \sim 1.4 \times 10^{63}$ cm^{-3}, where $EM \equiv \int n_e n_I \, dV$. Accounting for the presence of an additional thermal component of emission from the RS at $T \gg 20$ keV reduces the required EM to $EM_{FS} \sim 1.1 \times 10^{63}$ cm^{-3} and suggests $EM_{RS} \sim 4.3 \times 10^{62}$ cm^{-3}. To estimate the mass of the shocked CSM gas, we need to constrain the volume of the shocked CSM. Interpreting the occurrence of the peak of the emission at $t \sim 500$ days as due to the passage of the shock front through the CS shell, we constrain the shell thickness $R_{shell} \sim 10^{16}$ cm. The mass of the shocked CSM is thus $M_{CSM} \sim (1.0-1.5)$ $M_{\odot}$ with density $\rho_{shell} \sim 2 \times 10^6$ cm^{-3}. Introducing a volume filling factor f defined as $V_{shell} = 4\pi R_{shell}^2 \Delta R_{shell} f$, V_{shell}, the previous estimates would scale as $M_{CSM} \propto f^{1/2}$ and $\rho_{shell} \propto f^{-1/2}$.

The volume of the reverse post-shock layer between the RS and the contact surface can be easily computed considering that for $n = 9$, $R_{RS} = 0.92 \, R_{shell}$ (Chevalier & Liang 1989). For $EM_{RS} \sim 4.3 \times 10^{62}$ cm^{-3} the mass of the shocked SN ejecta is thus $M_{ej,RS} \sim 0.7 \, M_{\odot}$. As a sanity check, we note that momentum conservation implies that the mass of the CSM required to decelerate $\sim 0.7 \, M_{\odot}$ of SN ejecta with typical velocity $(2E_k/M_{ej})^{1/2} \gtrsim 10^4$ km s^{-1} down to ~ 4000 km s^{-1} is $M_{shell} \gtrsim 1.4 M_{ej,RS}$ or $M_{shell} \gtrsim 1 \, M_{\odot}$, consistent with our estimates above.

From another perspective, since the observed emission is dominated by the FS, the detected decrease of X-ray absorption with time (Figure 4) provides an independent constraint to the amount of neutral CSM material in front of the FS.[19] The detected temporal variation of NH_{tot} directly implies that the material responsible for the absorption is local to the SN explosion and within the reach of the SN shock over the timescale of our observations. From $t = 308$ days to 472 days after the explosion, we measure $NH_{tot} \sim 2 \times 10^{22}$ cm^{-2}. For $v_{FS} \sim 4000$ km s^{-1}, the detected NH_{tot} constrains the neutral CSM mass probed by the shock front between 308 days and 472 days to be $M_{CSM,NH} \sim 0.6 \, M_{\odot}$, while the total CSM shell mass is $\gtrsim 1.2 \, M_{\odot}$, assuming that the FS did not experience substantial acceleration and the CSM shell is spherical and homogeneous.

We end the section emphasizing the qualitative agreement of our conclusions, derived from a purely analytical treatment, with the results from the simulations from Chugai & Chevalier (2006). To reproduce the properties of SN 2001em, Chugai & Chevalier (2006) simulated the collision of freely expanding SN Ib/c ejecta with a dense shell of H-rich material at R_{shell}

---

[19]Note that the total amount of material is likely larger, as some material will be ionized.

= $(5–6) \times 10^{16}$ cm with thickness $\Delta R_{shell} \sim 10^{16}$ cm and $M_{shell} = (2–3)\ M_\odot$. The simulation thus differs from our situation only in terms of the larger CSM mass. These authors find that the SN ejecta interaction with the dense medium causes a large increase of L_x of both shocks, with L_x reaching $L_x \sim 10^{41}$ erg s^{-1} at peak. The FS, which was hotter than the RS before the strong interaction, experiences rapid deceleration, followed by a period of acceleration until the shock front reaches the edge of the shell. As a result, $T_{FS} \ll T_{RS}$ after the interaction (e.g., at $t = 1000$ days, $T_{FS} \sim 5$ keV and $T_{RS} \sim 100$ keV, and $T_{RS} \sim 850$ keV at $t = 500$ days, see their Figure 2). Compared to SN 2014C, the FS in the simulations by Chugai & Chevalier (2006) is more strongly decelerated by the impact with the CSM shell, due to the larger mass of the shell (the SN ejecta parameters are instead comparable). For the same reason, in their simulations, the peak of the X-ray emission due to the passage of the shock front through the CSM shell is also delayed with respect to SN 2014C (~1000 days, versus ~500 days). Apart from these expected differences, our analytical treatment captures the key physical properties of the SN ejecta—CSM strong interaction.

4.2.3. Anticipated Evolution at Later Times—The shock acceleration phase, caused by the increase of the pressure in the shocked region due to the interaction with the outer density profile of the SN ejecta, ends when (i) the RS reaches the flat portion of the ejecta profile; or (ii) the energy transmitted to the CSM shell becomes large compared to the energy of the shocked ejecta; or (iii) the shock front reaches the edge of the CSM shell (Chevalier & Liang 1989).

The timescale at which the RS reaches the bend in the SN ejecta profile is $t_1 \sim R_{RS}/v_0$, where $v_0 \equiv v_0\ (E_k, M_{ej}, n)$ is the transitional velocity that defines the SN ejecta profile and $v_0 \sim 10{,}700$ km s^{-1} for the explosion parameters of SN 2014C. Following Chevalier & Liang (1989), $t_1 \sim (R_{shell}\ /\ v_0)(1 + 3\ \gamma\ (\gamma - 1)\ ((\gamma + 1)(n - 5)))^{-1/3} \approx 0.92((R_{shell}\ v_0)$ for $n = 9$ and an adiabatic index $\gamma = 5/3$. For SN 2014C, we find $t_1 \gtrsim 550$ days. The timescale t_2 at which the energy transferred to the CSM gas is ≥0.5 the total energy in the shocked region is $t_2 \equiv t_2$ ($M_{ej}, E_k, n, \rho_{shell}, R_{shell}$). Employing the formalism by Chevalier & Liang (1989), their Equation (3.24), we find $t_2 > 550$ days for $\rho_{shell} \gtrsim 2 \times 10^6$ cm^{-3}. L_x reaches its maximum at $t < 500$ days (Figure 6), from which we deduce that the shock front already reached the edge of the high-density region by $t_3 \sim 500$ days. The later dynamics of the interaction is thus likely determined by this event, even if the timescales t_1 and t_2 are close enough that a simulation is needed to capture the details of the evolution.

Once the shock has transversed the dense shell, a rarefaction wave propagates into the interaction region, while the FS expands into a less dense medium that was shaped by the previous phase of evolution of the progenitor of SN 2014C. The simulations by Chugai & Chevalier (2006) show that the X-ray luminosity remains high even after the shell has been overtaken, but that the temperature of emission of both shocks declines with time. According to our calculations, for SN 2014C, the temperature of the RS shock will enter the *NuSTAR* passband at $t > 800$ days ($T_{RS} \sim 100$ keV at $t \sim 800$–1000 days, depending on the ionization state of the ejecta). Future observations will allow us to sample the density of the CSM outside the dense shell. At the moment we note that optical spectroscopy of SN 2014C (M15) reveals that the material outside the CSM shell is H-rich and shows velocities of <100 km s^{-1} (from the narrow component of the Hα line, Figure 10). These velocities are typical

of winds emanating from non-compact progenitors and are typically associated with the large mass-loss rates (and densities) inferred for type IIn SNe (e.g., Kiewe et al. 2012). It is thus possible that the shocked gas will never re-enter a phase of free expansion.

4.2.4. Clumpy Structure of the CSM—Two independent sets of observations point to a complex structure of the interaction region with overdense clumps of emitting material: (i) the velocity profile of the shocked H-rich material and (ii) the presence of prominent Fe emission lines in the X-ray spectra.

Optical spectroscopy in Figure 10 (see M15 for details) shows velocities of <2000 km s^{-1} for the shocked H-rich material, while above we infer $v_{FS} \sim 4000$ km s^{-1} for the expansion of the shock front at the same epoch. These two results can be reconciled if the H-rich material that dominates the Hα emission is clumpy and is concentrated in regions with

density contrast $\rho_{\mathrm{clumos}}/\rho_{\mathrm{shell}} \sim (v_{\mathrm{FS}}/v_{\mathrm{H}_{\alpha}})^2 \approx 4$.

Astrophysical plasmas with $T < 3 \times 10^7$ K produce a forest of X-ray lines. At higher temperatures, line emission is inhibited and cooling is dominated by bremsstrahlung. At $T \sim$ 20 keV ($\sim 2 \times 10^8$ K), the only transitions that survive are those associated with extremely ionized states of Fe atoms, i.e., He-like and H-like Fe atoms. Consistent with these expectations, in each epoch of observation, we clearly identify a localized excess of X-ray emission at ~ 6.7–6.9 keV that we associate with He-like and H-like Fe atoms transitions (Figures 4 and 5). However, a single-temperature, collisionally ionized plasma model in thermal equilibrium fails to reproduce the observed luminosity of the Fe emission at all epochs. At temperature ~ 20 keV and density $\sim (2$–$4) \times 10^6$ cm^{-3} the time for electrons and protons to come into equilibrium is $t_{ei} < t_{obs}$ and $t_{ei} \sim 80$ days (Spitzer 1962), justifying our assumption of thermal equilibrium so far. A way to reconcile the prominent Fe emission within this model is to invoke super solar abundances (~ 5 times the solar value) for the shocked CSM shell. Alternatively, observations are consistent with a multi-phase plasma, with a lower temperature (and higher density) component responsible for the Fe emission. Given the independent suggestion of a clumpy medium from the Hα velocity profile, we consider this second possibility of a medium with components of different densities (and not necessarily spherically simmetric) more likely.

Evidence or hints for an excess of emission around 6.7–6.9 keV has been found in some SNe characterized by strong interaction with a dense medium. Examples include the type-IIn SNe 1996cr (Dwarkadas et al. 2010; Dewey et al. 2011), 2006jd (Chandra et al. 2012), and SN 2009ip (Margutti et al. 2014a). In all cases, the excess has been interpreted as originating from H-and He-like transitions of collisionally ionized Fe atoms. Interestingly, in the case of SN 2006jd, Chandra et al. (2012) arrived to a similar conclusion of either a very enriched medium with super solar abundances or a multi-phase plasma to explain the luminous Fe emission.

5. SN 2014C in the Context of 183 Ib/c SNe with Radio Observations

5.1. Rate of 14C-like Explosions Among Ib/c SNe

In this section, we quantify how common 14C-like radio re-brigthenings are among H-stripped core-collapse SNe by using published radio data. We focus on the radio wavelength range because it currently offers the most homogeneous data set. Our sample comprises public observations of 183 type Ib/c SNe obtained over more than 20 years, with data acquired from a few days to ~32 years since explosion (Table 5). The data have been collected from Berger et al. (2003), Soderberg et al. (2006), Soderberg (2007), Bietenholz et al. (2014), Corsi et al. (2014), Kamble et al. (2014), Drout et al. (2015), and references therein. In 41 cases, radio observations provide meaningful constraints to the presence of a 14C-like radio rebrightening (i.e., the observations are deep enough and cover the late-time evolution of the transient at $t \gtrsim 500$ days). For the remaining 142 SNe Ib/c, the available observations do not reach the necessary depth and/or do not extend to late times.

Out of 41 type Ib/c SNe with good radio coverage, we can rule out a 14C-like radio rebrightening in 37 cases. For the type Ib/c SNe 2001em (Bietenholz & Bartel 2005; Schinzel et al. 2009), 2003gk (Bietenholz et al. 2014), 2007bg (Soderberg 2007; Salas et al. 2013), and PTF11qcj (Corsi et al. 2014), we find evidence for late-time, luminous radio re-brightenings consistent with a 14C-like phenomenology (Figure 9). In particular, we note that (i) albeit sparsely sampled, the X-ray and optical evolution of the type-Ic SN 2001em (Filippenko & Chornock 2001) are also reminiscent of SN 2014C (Chugai & Chevalier 2006) and (ii) we further point out the possible detection of an outburst from the stellar progenitor of PTF11qcj ~2.5 years before the explosion (Corsi et al. 2014). We thus conclude that ~10% of Ib/c SNe with constraining radio observations displays late-time radio re-brigthenings reminiscent of SN 2014C and that, when available, multi-wavelength observations of this subset of SNe independently support the idea of an enhanced mass loss from the progenitor star during the last stages of evolution preceding core collapse. We note that while this sample has been collected from different sources, there is no obvious observational bias that would favor a larger fraction of interacting systems. In fact, radio SNe tend to be followed up at later times in the case of an early-time radio detection, which suggests that we might have missed later time radio re-brightenings in systems with faint or undetected early emission. This source of bias is alleviated in part by the fact that some SNe in our sample have been followed up at early and late times (irrespective from a detection of lack thereof) as part of the searches for off-axis emission from a Gamma-Ray Burst-like jet. We quantify this source of uncertainty in the next paragraph.[20]

In Figure 8, we summarize our analysis of the enlarged sample of 60 Ib/c SNe with radio observations sensitive enough to detect re-brightenings with similar luminosity to SN 2014C (i.e., we relaxed the condition of a radio monitoring extending to late times $t \gtrsim 500$ days of the previous paragraph). This plot shows that existing radio observations rule out the presence of strong interaction in a large fraction of Ib/c SNe only at early times (e.g., for $t \lesssim$

---

[20]There are SNe (e.g., SNe 1986J and 1996cr, Rupen et al. 1987; Dwarkadas et al. 2010) that have been discovered at late times from their bright radio emission and classified as type IIn events from their late-time spectra. These events are not part of this sample by definition. However, they might have been classified as type Ib/c SNe if early optical spectra had been available.

100 days, ≳80% of Ib/c SNe do not show evidence for strong shock interaction), while at later times the phase space is sparsely sampled, so that we can exclude a 14C-like behavior at $t \gtrsim 1000$ days only for ~40% of the SNe.

SN 2014C represents an extreme case of radio flux variability. Small-scale radio light-curve modulations at the level of a factor of ~2 in flux are common and found in ~50% of SNe Ib/c with radio detection (see also Soderberg 2007). This phenomenology can be explained within the context of turbulence-driven small-scale clumping of the stellar wind (Moffat 2008), a physical process that generates moderate density variations of a factor of ~2–4. The "bubble plus thick shell structure" that we infer for SN 2014C clearly demands a different origin. More pronounced achromatic radio flux variations due to modulations of the environment density of a factor of ~3–6 have been observed in SNe 2004cc, 2004dk, and 2004gq (Wellons et al. 2012). In particular, the radio light curve of SN 2004cc shows a well-defined double-peaked structure with a flux contrast of ~10, a first peak of emission at ~25 days, and a second radio peak at ~150 days since the explosion (Wellons et al. 2012, their Figure 1). While this behavior is somewhat reminiscent of SN 2014C, the radio flux from SN 2004cc rapidly and significantly faded on a timescale of $\delta t/t \lesssim 1$, pointing to a smaller mass of the dense region encountered by the SN shock. This comparison highlights the fact that, among type Ib/c SNe, 14C-like events might represent the most extreme manifestations of a more common physical process that induces severe progenitor mass loss synchronized with the final explosion on a variety of mass-loss scales. With this notion in mind, in the following, we concentrate on the nature of 14C-like SNe.

5.2. Statistical Inference on the Nature of the Underlying Physical Process

Current radio studies efficiently sample the first $t \sim 500$ days of evolution of Ib/c SNe (Figure 8). For a typical shock velocity of ~0.15 c, we are thus currently systematically exploring a region of ~2×10^{17} cm around Ib/c SNe. For a medium that has been enriched by material ejected by the stellar progenitor with velocity v_w, this fact implies that we are effectively sampling $t_{sampled} \sim 60 \times (v_w/1000 \text{ km s}^{-1})^{-1}$ years of life of the massive progenitor star before the explosion. This value corresponds to a very small fraction $f < 2 \times 10^{-3}$ of the entire life span τ of a massive star, even in the case of slowly moving material with $v_w = 10$ km s^{-1} and a very massive progenitor with a short life of $\tau \sim 3$ Myr. We consider $v_w = 10$–1000 km s^{-1} to be a representative range of velocities of the ejected material. Velocities of the order of $v_w \sim 10$ km s^{-1} are expected in the case of CE ejection by a binary system, while $v_w \sim 1000$ km s^{-1} are the typical wind velocities observed in Wolf-Rayet stars.

The observed fraction of 14C-like objects is $\gg f$ (Section 5.1), which implies that 14C-like mass ejections preferentially occur toward the end of the life of the stellar progenitor. We will refer to the interval of stellar life time during which a mass ejection can occur as the progenitor "active time" (t_{active}). The physical process responsible for the mass ejection is thus closely synchronized with the stellar death.

The results from Section 5.1 are statistically consistent with two scenarios. (i) We are sampling a representative portion of t_{active} of Ib/c SN progenitors and $t_{active} \sim t_{sampled}$. 14C-like mass ejections are intrinsically rare and only happen in a limited fraction (~10%)

of progenitors under peculiar circumstances. (ii) $t_{active} \gg t_{sampled}$, all Ib/c SN progenitor stars experience an active phase and the small sample of Ib/c SNe with evidence for strong interaction is a mere consequence of our incomplete sampling of the previous stages of stellar evolution. If this is the case, $t_{active} \sim 500 \times (v_W/1000 \text{ km s}^{-1})$ years. The minimum and maximum t_{active} consistent with the detection of four strong radio re-brigtenings out of a sample of 41 Ib/c SNe can be easily derived from a binomial distribution with $p = t_{sampled}/t_{active}$, where p is the probability of success (e.g., Romano et al. 2014). For $v_W = 1000 \text{ km s}^{-1}$ we find 200 year $< t_{active} < 5000$ year (3σ confidence level), while for $v = 10 \text{ km s}^{-1}$, we find 22,000 year $< t_{active} < 500,000$ year. We consider hypothesis (ii) to be the most likely scenario, since we are only sampling a limited portion of the parameter space and we have no reason to believe that the portion that we are sampling is truly representative of the entire distribution.

6. Interpretation and Discussion: Massive Star Evolution Revised

6.1. A Continuum of Stellar Explosions between Type Ib/c and Type-IIn SNe

SN 2014C evolved from an ordinary SN Ib to a strongly interacting type-IIn SN over ~1 year (Figure 10). The location of the dense H-rich shell at $R \sim 5.5 \times 10^{16}$ cm indicates a mass ejection ~20(v_H/1000 km s^{-1}) years preceding the explosion, where v_H is the ejection velocity of the shell. The H-rich shell was far enough from the explosion site not to be efficiently ionized by the SN shock and radiation during the first ~100 days (M15)—which allowed the early SN classification as an H-poor, type Ib event, but close enough for the shock-CSM interaction to develop on timescales that are relevant to our coordinated monitoring—which allowed us to witness the later transition to type IIn SN—(Figure 11). Our results thus further reinforce the picture that stars that are progenitors of normal H-stripped SNe experience enhanced mass loss before collapsing, as it was recently suggested for the type-IIb SN 2013cu (using flash spectroscopy, which probes a more nearby region around the stellar explosion $R \sim 10^{15}$ cm, Gal-Yam et al. 2014).

A key difference between ordinary IIn SNe-and 14C-like events lies in the location of the H-rich material, which maps into a different epoch of H-envelope ejection. Type IIn SNe are characterized by strong interaction with dense CSM since the very first moments after the explosion, which requires a very recent ejection of H-rich material (typically within a few years before the stellar demise) and results in the H-rich material being at $R < 10^{16}$ cm from the explosion center.[21]

Recent observations indeed provided direct evidence for eruptive behavior of progenitors of type IIn-like SNe in the years to days before a major explosion (e.g., Fraser et al. 2013; Mauerhan et al. 2013a; Ofek et al. 2013, 2014; Pastorello et al. 2013; Prieto et al. 2013; Margutti et al. 2014a; Smith 2014). Our observations of SN 2014C suggest that a fraction of SNe spectroscopically classified of type IIn in fact contained bare type Ib/c-like cores that recently ejected their H envelopes. This suggestion would naturally account for the diverse

---

[21]It is important to keep in mind that IR observations of type-IIn SNe revealed that, in addition to the very recent H-rich mass loss, type-IIn progenitors also experience massive shell ejections in the decades to hundreds of years prior to the SN explosion (Smith et al. 2008; Miller et al. 2010; Fox et al. 2013).

environments of IIn SNe (which argue for a broad range of progenitor star masses; Kelly & Kirshner 2012; Anderson et al. 2015; Taddia et al. 2015) and it is in line with what was inferred for the type-IIn SN 1996cr (Dwarkadas et al. 2010). In general, our picture would explain the observational properties of type-IIn SNe like 1986J that did not show evidence for high-velocity H features during its spectroscopic evolution, but showed evidence for broad O features at late times (Rupen et al. 1987; Bietenholz et al. 2002; Milisavljevic et al. 2008). Finally, the diversity of the multi-wavelength light curves of type-IIn SNe, particularly at optical wavelengths is also suggestive of a range of type-IIn progenitors (Fox et al. 2013).

Previous studies pointed to a continuum of properties among SNe interacting with He-rich and H-rich material (i.e., type-Ibn SNe and SNe of type IIn, Smith et al. 2012; Pastorello et al. 2015 and references therein). With our study, we significantly extend the continuum to include even H-stripped core-collapse explosions. The existence of 14C-like events argues in favor of a continuum of stellar explosions that bridges the gap between Ib/c and IIn SNe (Figure 11) and that directly maps into a continuum of timescales of ejection of the H-rich envelope of progenitors of H-stripped SNe, extending from less than one year to thousands of years before explosion.

6.2. The Origin of the H-rich Shell in SN 2014C

SN 2014C is an ordinary H-poor SN embedded in a nonstandard H-rich environment. Here we discuss the origin of the H-rich, dense CSM material around SN 2014C in the context of the stellar evolution and mass-loss mechanisms of evolved massive stars.

Single massive stars that are progenitors of ordinary H-stripped SNe are expected to evolve from H-rich, extended Red SuperGiants (RSGs) into core-He-burning compact Wolf-Rayet (WR) stars ~0.5–1 Myr before exploding as H-poor SNe (e.g., Heger et al. 2003). The presence of H-rich material within $\sim 6 \times 10^{16}$ cm of the explosion site of SN 2014C demands an exceptionally short WR phase of its progenitor star, lasting only ~20 years (for an ejection velocity of the H-rich material $v_H = 1000$ km s^{-1}), and a very large mass-loss rate during the previous RSG phase $\dot{M}_{\rm RSG} \geqslant 7 \times 10^{-4} M_\odot \, {\rm yr}^{-1}$ (the inequality accounts for the fact that the RSG wind is in fact freely expanding). This value is ~10 times larger than the typically observed mass-loss rates during the RSG phase (observations indicate $\dot{M}_{\rm RSG} < 10^{-4} M_\odot \, {\rm yr}^{-1}$, van Loon et al. 2005; Mauron & Josselin 2011) and exceeds the limit for mass loss due to the commonly assumed line-driven winds even in the case of a small filling factor $f = 0.1$ of the H-rich shell (e.g., Smith 2014, their Figure 3). This scenario is explored in M15.[22]

---

[22]Another possibility is that SN 2014C exploded in an environment enriched by its stellar companion. This scenario would require having an ordinary SN Ib/c exploding within ~20 years of a giant LBV-like eruption from its stellar companion by chance. Non-terminal, giant eruptions are typically associated to very massive stars (i.e., Luminous Blue Variable stars, LBV, Humphreys & Davidson 1994), which would require the progenitor of SN 2014C to be even more massive in order to exhaust its H fuel and explode before its companion. The standard explosion properties of SN 2014C and its ordinary luminosity do not support this scenario (Section 3 and Figure 7). Furthermore, this picture is unlikely to be able to account for the entire fraction of ~10% of SNe Ib/c that present a 14C-like behavior (Section 5.1).

We thus conclude that SN 2014C violates several expectations from evolutionary models that employ time averaged mass-loss prescriptions and do not include highly time-dependent mass-loss episodes associated with instabilities during the last stages of stellar evolution and the effects of binarity. With SN 2014C, we further have clear evidence that mass-loss mechanisms other than the commonly assumed metallicity-dependent line-driven winds are active and play an important role in the process that leads to the H-stripped progenitors of SNe Ib/c. This picture, if common among Ib/c SN progenitors, naturally explains why the mass-loss rates inferred for the progenitors of SNe Ib/c span a much larger range than the observed wind mass-loss rates of WRs in our Galaxy (e.g., Soderberg 2007; Wellons et al. 2012). Finally, the indication of non-metallicity driven mass-loss mechanisms being at play in the evolutionary path that leads to Ib/c SNe is also consistent with inferences from the demographics of SN types combined with initial-mass function considerations (Smith et al. 2011).[23]

To explain the observations of SN 2014C, we explore below the possibility of alternative physical mechanisms responsible for the ejection of the H envelope of its progenitor, with three key requirements: (i) synchronized with the explosion, (ii) efficient and able to (almost) entirely strip the star of its last H layer, (iii) common to 10% of progenitors of H-stripped SNe during their last ~500 years of evolution, but potentially to every SN Ib/c progenitor if the process is intrinsically active over a longer timescale of 5000 years or more.

6.2.1. Binary Interaction—The ejection of the H-rich envelope can result from binary interaction (e.g., Podsiadlowski et al. 1992). Since the majority of young massive stars resides in interacting binary systems (e.g., Sana et al. 2012), these ejections are expected to be common, but not necessarily synchronized with the stellar death. The binary interaction can strip the star of almost all of its H, leaving behind just a thin H layer on its surface (which would be later lost through metallicity-dependent, line-driven winds, consistent with what we observe for SN 2014C). We note that a binary progenitor for SN 2014C is independently suggested by the pre-explosion observations of the cluster of stars that hosts SN 2014C, which favor lower-mass star progenitors with $M < 20\ M_\odot$ (M15). Finally, since the observed fraction of ~37% of H-poor SNe among core-collapse explosions is too large to be reconciled with the evolution of single massive stars (e.g., Kobulnicky & Fryer 2007; Eldridge et al. 2008; Li et al. 2011; Smith et al. 2011), it is expected that at least a fraction of SNe Ib/c originate in binaries.

However, we do not expect the stellar death and the binary interaction to be synchronized in time. The time lag can be small if the progenitor fills its Roche lobe in a late evolutionary stage. This occurs for systems with orbital periods longer than ~1000 days that undergo case-C mass transfer (e.g., Figure 1 in Schneider et al. 2015). In such systems, the progenitor fills its Roche lobe as an RSG, after central He burning, a few thousands years before collapse. The convective envelope responds to mass loss by expanding, leading to dynamically unstable mass transfer in which the companion is engulfed in the envelope. The envelope is ejected as the companion spirals in, which takes a few orbits at most (Ivanova et

---

[23]See Modjaz et al. (2011), Modjaz (2012), Leloudas (2012), and Sanders et al. (2012) for a statistical study of the metallicity at the explosion site of type-Ib and Ic SNe.

al. 2013). This means that several solar masses of hydrogen-rich material are ejected within a short time ($\lesssim$1 year), leading to a dense shell, torus, or disk around the binary system.

The outflow velocities of the H-rich material are expected to be comparable to the escape speed of the surface of the RSG (up to a few 10 km s^{-1}, e.g., Ivanova et al. 2013), or possibly even less if the material remains bound to the system and resides in a circum-binary disk. Material with higher velocity might be found along the poles if the system develops a bipolar geometry (Soker 2015). It is unclear how long the ejected material can survive in the vicinity of the system. The ejected material will be shaped and eventually eroded by the fast line-driven wind of the stripped progenitor and its ionizing photons (Metzger 2010).

Case-C mass transfer is relatively rare for binary systems where the primary is massive enough to produce an SN. Podsiadlowski et al. (1992) estimate this fraction to be ~6% among binary systems with primaries with masses in the range of 8–20 $M_\odot$. To quantify the uncertainty affecting this estimate and understand the impact of different assumptions, we use the binary star population synthesis code binary_c (Izzard et al. 2004, 2006, 2009; de Mink et al. 2013), which relies on the algorithms by Hurley et al. (2000, 2002). The crucial ingredients in this estimate are the stellar lifetimes and radial expansion of the stars, which follow from the detailed stellar evolutionary models by Pols et al. (1998). These algorithms provide a computationally efficient approximation that allows us to simulate a full population of binary systems. The approximations are sufficient for the scope of this work, but future investigation with detailed codes would be desirable.

We simulate binary populations by choosing primary masses from a Kroupa (2001) mass function and companion masses uniformly distributed with a mass ratio between 0.1 and 1 (e.g., Sana et al. 2012; Duchêne & Kraus 2013). We assume a uniform distribution of initial periods p in log space (Öpik's law). However, for systems with initial masses above 15 $M_\odot$, we adopt the distribution obtained by Sana et al. (2012) that more strongly favors short period systems, with $0.15 \leq \log_{10} p \leq 3.5$. We assume a binary fraction of 0.7. We account for the relevant physical processes that govern binary systems including stellar wind mass loss, Roche-lobe overflow, and common envelope (CE) phases using the standard assumptions for the physics parameters as summarized in de Mink et al. (2013) and references therein. In addition, apart from our standard model, we also run simulations with different assumptions for the initial conditions (i.e., slope of the initial-mass function, binary fraction, distribution of mass ratios, and orbital periods) and the treatment of the physical processes (i.e., efficiency of CE ejection, efficiency of mass transfer, critical mass ratio for the onset of contact, amount of mixing, and mass loss assumed during a stellar merger). We find that the variations in the initial-mass function dominate the uncertainty. We refer to de Mink et al. (2013), de Mink et al. (2014), and Izzard et al. (2004) for a detailed discussion. The full set of simulations will be published in E. Zapartas et al. (2017, in preparation).

We find that ~6.5% (3.8%–10%) of type Ib/c SN progenitors results from systems that experienced case-C CE evolution. The 3.8%–10% range reflects a variation of the slope of the initial-mass function $a_{\mathrm{IMF}} = -2.3 \pm 0.7$. The other parameters of our model induce smaller variations to the final fraction of progenitors that went through case-C CE evolution. The fraction of progenitors with recent CE evolution is thus reasonably close to our

estimates of interacting systems of Section 5. The typical progenitors are stars of 8–20 $M_\odot$ in wide binary systems of $\gtrsim 1000$ days, which experience unstable mass transfer and CE after their core He exhaustion. At this stage, the life time before core collapse is similar to the timescale for carbon burning, which is typically a few 10^3 years, but potentially extends to a few 10^4 years for the lowest-mass progenitors (Jones et al. 2013). This fact implies that binary interaction can be the main culprit if the material ejected during the CE phase is able to survive close to the system for a few $\sim 10^3$–10^4 years.

Alternatively, we need to invoke a new physical mechanism to enhance the fraction of Ib/c SNe with CE interaction shortly before the explosion. A possibility is to consider exotic binary evolutionary channels where the final explosion has a causal relation with the binary interaction. One example is the reverse CE inspiral of a neutron star or black hole in the envelope of the companion as discussed by Chevalier (2012). Based on the estimates by Chevalier (2012), this channel would be able to account for 1%–3% Ib/c SNe. Alternatively, the fraction of interacting systems can be increased if the stellar radius of the progenitor inflates before the explosion.[24] Instabilities during the last phases of nuclear burning evolution might inject the necessary energy that leads to envelope inflation and binary mass transfer prior to explosion (Soker 2013; Mcley & Soker 2014; Smith & Arnett 2014) and might explain the larger fraction of interacting Ib/c supernovae in our sample.

6.2.2. Instabilities during the Final Nuclear Burning Stages—Instabilities

associated with the final nuclear burning sequences (especially O and Ne) have recently been invoked to explain the observation of eruptions from massive stars in the months to years before core collapse (Arnett & Meakin 2011b; Quataert & Shiode 2012; Shiode et al. 2013; Shiode 2013; Smith & Arnett 2014). In the case of lower-mass stars with $M \sim 10~M_\odot$, (which is more relevant to SN 2014C), Woosley et al. (1980) and Woosley & Heger (2015) discuss the possibility of violent flashes at the onset of Silicon ignition with sufficient energy to eject the H envelope of the star many months before core-collapse. These mechanisms are naturally synchronized with the stellar demise and it is expected to be common to most stars. Our observations of SN 2014C require the H envelope ejection to have happened ≥ 20 years before the explosion, which means before the start of the O-burning phase. Heavy mass loss in the H-stripped SN 2014C was thus not limited to the few years preceding the collapse, and, if connected to nuclear burning instabilities, (i) directly points to the development of instabilities even at earlier times in the nuclear burning sequence and (ii) must accommodate for the almost complete stripping of the H envelope.

Current theoretical investigations have explored with realistic simulations only the very late nuclear burning stages (O, Ne, and later stages, with duration of the order of approximately years) mainly because of limitations in computational power (Meakin 2006; Arnett & Meakin 2011a; Smith & Arnett 2014; Smith 2014). SN 2014C and our analysis of type Ib/c SNe of Section 5.2 is, however, suggestive of a significantly longer active time of the physical process behind the ejection of massive H-rich material. For $v_H \ll 1000$ km s^{-1},

---

[24]We note that envelope inflation due to nuclear activity has been suggested during other pre-collapse evolutionary stages as well, see, e.g., Bear et al. (2011).

$t_{\text{active}} \gg 5000$ years, thus extending well back into the C-burning stage of massive stars (e.g., Yoon & Cantiello 2010; Shiode & Quataert 2014).

Two sets of independent observations are relevant in this respect. First, while the exact timescales of each burning stage is sensitive to the currently imposed mass-loss rates in stellar evolution models, which do not include the effects of time-dependent mass loss discussed in this section, the detection of infrared echoes from distant shells in the environments of IIn (e.g., Smith et al. 2008, 2010b; Miller et al. 2010; Fox et al. 2011, 2013) and non-IIn SNe (an illustrative example is the ring of material at $\sim 6 \times 10^{17}$ cm from the explosion site of SN 1987A, Sonneborn et al. 1998) independently supports the idea that enhanced mass loss is not confined to the few years before the stellar collapse. Second, the idea that instabilities at the onset of C-burning might be triggering eruptions has been suggested by the statistical analysis of massive shells around luminous stars in our Galaxy (Kochanek 2011) and by the study of ηCarinae analogs in nearby galaxies (Khan et al. 2015).

It is thus urgent to theoretically explore the possibility of instabilities during the earlier stages of nuclear burning, potentially extending to C-burning. The, so far, neglected time dependence of nuclear burning and mass loss in massive stars might have a fundamental influence on the pre-SN structure of the progenitor star, a key input parameter to all numerical simulations of SN explosions (Janka 2012).

7. Summary and Conclusions

SN 2014C represents the first case of an SN originating from an H-stripped progenitor for which we have been able to closely monitor a complete metamorphosis from an ordinary Ib-SN into a strongly interacting type-IIn SN over a timescale of ~1 year. Observational signatures of this evolution appear across the electromagnetic spectrum, from the hard X-rays to the radio band. The major finding from our study of SN 2014C is the presence of substantial ($M \sim 1\ M_{\odot}$) H-rich material located at $R \sim 6 \times 10^{16}$ cm from the explosion site of an H-poor core-collapse SN. This phenomenon challenges current theories of massive stellar evolution and argues for a revision of our understanding of mass loss in evolved massive stars. Specifically:

1.   With $E_{\text{k}} \sim 1.8 \times 10^{51}$ erg, $M_{\text{ej}} \sim 1.7\ M_{\odot}$ and $M_{\text{Ni}} \sim 0.15\ M_{\odot}$, the explosion parameters of SN 2014C are unexceptional among the population of Ib/c SNe.

2.   SN 2014C adds to the complex picture of mass loss in massive stars that recent observations are painting (Smith 2014) and demonstrates that the ejection of massive H-rich material is not a prerogative of very massive H-rich stars ($M \sim 60\ M_{\odot}$, like the progenitor of SN 2009ip, Smith et al. 2010b; Foley et al. 2011). Instead, it shows that even progenitors of normal H-poor SNe can experience severe pre-SN mass loss as late as $10 \lesssim t \lesssim 1000$ years before explosion. Heavy mass loss in SNe Ib/c is thus not limited to the few years preceding core collapse.

3.   In this sense, SN 2014C bridges the gap between ordinary SNe Ib/c and type-IIn SNe, which show signs of shock interaction with a dense medium from the very beginning. The existence of 14C-like events establishes a continuum of

timescales of ejection of substantial H-rich material by massive stars, extending from <1 year before collapse for type-IIn SNe, to decades and centuries before explosion for Ib/c SNe. This fact leads to the idea that a fraction of spectroscopically classified type-IIn SNe, in fact, harbor bare Ib/c-like cores that underwent a very recent ejection of their H-rich envelopes.

4.   SN 2014C violates the expectations from the standard metallicity-dependent line-driven mass-loss channel and demonstrates the existence of a time-dependent mass-loss mechanism that is active during the last centuries of evolution of some massive stars and that leads to progenitors of ordinary H-poor core-collapse SNe. Possibilities include the effects of the interaction with a binary companion or instabilities during the last nuclear burning stages. In both cases, we do not expect a strong metallicity dependence.

5.   We analyzed 183 Ib/c SNe with radio observations and we found that 10% of SNe in our sample displays evidence for late-time interaction reminiscent of SN 2014C. This fraction is somewhat larger than—but in reasonable agreement with—the expected outcome from recent envelope ejection due to binary evolution, assuming that the envelope material can survive close to the progenitor site for 10^3–10^4 years. Alternatively, events related to the last phases of nuclear burning might also play a critical role providing the energy and the trigger mechanism that cause the ejection of envelope material from an evolved massive star.

6.   In particular, our observations indicate that unsteady nuclear burning (i) may be spread across a wide range of initial progenitor mass that includes the progenitors of normal Ib/c SNe; (ii) instabilities are not confined to the O, Ne, and Si-burning phases, but instead likely extend all the way to C-burning; (iii) unsteady nuclear burning might enhance the fraction of binary interactions before collapse.

These findings highlight the important role of time-dependent, eruptive mass loss in the evolutionary path that leads to the progenitors of ordinary H-poor core-collapse SNe. The incorrect use of time averaged mass-loss prescriptions in current models of stellar evolution might have a major effect on our understanding of the stellar structure of a massive stellar progenitor approaching core collapse and might lead to inaccuracies in pre-SN stellar structure that are of fundamental importance at the time of the explosion. To make progress, it is urgent to theoretically explore the presence of instabilities during the earlier stages of nuclear evolution in massive stars, and, in general, to study the effects of significant eruptive mass loss on the pre-supernova stellar structure. Observationally, it is mandatory to consistently sample the pre-SN life of stellar progenitors in the centuries before explosion, a territory that can only be probed with late-time radio and X-ray observations of nearby stellar explosions.

Acknowledgments

Appendix

Table 5 presents the list of radio supernovae from the hydrogen-stripped progenitors considered for this study.

Table 5

Sample of 183 Ib/c SNe with Radio Observations

1954A	1983N	1984L	1985F	1990B	1990U	1991A	1991N	1991ar
1994I	1994ai	1996D	1996aq	1997B	1997C	1997X	1997dc	1998bw
1998T	1999bc	1999di	1999dn	1999ec	1999eh	1999ex	2000C	2005C
2000F	2000H	2000S	2000ds	2000dv	2000cr	2000ew	2000fn	2001B
2001M	2001ai	2001bb	2001ch	2001ci	2001ef	2001ej	2001em	2001is
2002J	2002ap	2002bl	2002bm	2002cj	2002cp	2002dg	2002dn	2002ge
2002gy	2002hf	2002hn	2002ho	2002hy	2002hz	2002ji	2002jj	2002jp
2002jz	2003I	2003L	2003ih	2003kb	2003jg	2003jd	2003is	2003ig
2003hp	2003id	2003gk	2003gf	2003ev	2003el	2003ds	2003dr	2003dg
2003cr	2003bu	2003bp	2003bm	2003aa	2003I	2003H	2003A	2004ao
2004ax	2004aw	2004bf	2004bi	2004bm	2004bs	2004bw	2004bu	2004cc
2004dc	2004dk	2004dn	2004dx	2004eh	2004eu	2004fe	2004ff	2004ge
2004gk	2004gq	2004gt	2004gv	2005E	2005C	2005V	2005N	2005O
2005aj	2005ar	2005az	2005bf	2005bh	2005bj	2005bk	2005bq	2005ce
2005ct	2005da	2005cz	2005dg	2005ek	2005eo	2005hg	2005ke	2005kl
2005kf	2005kz	2005la	2005lr	2005mf	2005nb	2006F	2006ab	2006bf
2006bk	2006cb	2006ck	2006dj	2006dl	2006dg	2006dn	2006ea	2006eg
2006ei	2006ec	2006ep	2006el	2006fo	2006gi	2006jc	2006lt	2007C
2007D	2007I	2007Y	2007bg	2007cl	2007gr	2007iq	2007ke	2007ru
2007rz	2007uy	2008D	2008du	2008dv	2009bb	2010ay	PTF11qcj	2012ap
2012au	2013ge	2014ad	…	…	…	…	…	…

References

Anderson JP, James PA, Habergham SM, Galbany L, Kuncarayakti H. PASA. 2015; 32:19.

Arnett WD. ApJ. 1982; 253:785.

Arnett WD, Meakin C. ApJ. 2011a; 733:78.

Arnett WD, Meakin C. ApJ. 2011b; 741:33.

Bastian N, Covey KR, Meyer MR. ARA&A. 2010; 48:339.

Bear E, Soker N, Harpaz A. ApJL. 2011; 733:L44.

Berger E, Kulkarni SR, Frail DA, Soderberg AM. ApJ. 2003; 599:408.

Bietenholz MF, Bartel N. ApJL. 2005; 625:L99.

Bietenholz MF, Bartel N, Rupen MP. ApJ. 2002; 581:1132.

Bietenholz MF, De Colle F, Granot J, Bartel N, Soderberg AM. MNRAS. 2014; 440:821.

Björnsson CI, Fransson C. ApJ. 2004; 605:823.

Brown PJ, et al. AJ. 2009; 137:4517.

Burrows DN, et al. SSRv. 2005; 120:165.

Cano Z. MNRAS. 2013; 434:1098.

Cano Z, Jakobsson P. arXiv. 2014; 1409:3570.

Cano Z, Maeda K, Schulze S. MNRAS. 2014; 438:2924.

Cardelli JA, Clayton GC, Mathis JS. ApJ. 1989; 345:245.

Chandra P, Chevalier RA, Chugai N, et al. ApJ. 2012; 755:110.

Chevalier RA. ApJ. 1982; 258:790.

Chevalier RA. ApJ. 1984; 280:797.

Chevalier RA. ApJL. 2012; 752:L2.

Chevalier RA, Fransson C. ApJ. 2006; 651:381.

Chevalier RA, Liang EP. ApJ. 1989; 344:332.

Chugai NN, Chevalier RA. ApJ. 2006; 641:1051.

Clocchiatti A, Wheeler JC. ApJ. 1997; 491:375.

Corsi A, et al. ApJ. 2014; 782:42.

Crowther PA. ARA&A. 2007; 45:177.

de Jager C, Nieuwenhuijzen H, van der Hucht KA. A&AS. 1988; 72:259.

de Mink SE, Langer N, Izzard RG, Sana H, de Koter A. ApJ. 2013; 764:166.

de Mink SE, Sana H, Langer N, Izzard RG, Schneider FRN. ApJ. 2014; 782:7.

Dewey, D., Bauer, FE., Dwarkadas, VV. AIP Conf Ser 1358. McEnery, JE.Racusin, JL., Gehrels, N., editors. Melville, NY: AIP; 2011. p. 289

Drout MR, et al. ApJ. 2011; 741:97.

Drout MR, et al. ApJ. 2016; 821:57.

Duchêne G, Kraus A. ARA&A. 2013; 51:269.

Dwarkadas VV. ApJ. 2005; 630:892.

Dwarkadas VV. Ap&SS. 2007; 307:153.

Dwarkadas VV, Dewey D, Bauer F. MNRAS. 2010; 407:812.

Eldridge JJ, Izzard RG, Tout CA. MNRAS. 2008; 384:1109.

Falk SW, Arnett WD. ApJS. 1977; 33:515.

Filippenko AV, Chornock R. IAUC. 2001; 7737:3.

Foley RJ, Berger E, Fox O, et al. ApJ. 2011; 732:32.

Foley RJ, Smith N, Ganeshalingam M, et al. ApJL. 2007; 657:L105.

Fox OD, Filippenko AV. ApJL. 2013; 772:L6.

Fox OD, Filippenko AV, Skrutskie MF, et al. AJ. 2013; 146:2.

Fox OD, et al. ApJ. 2011; 741:7.

Fransson C, Lundqvist P, Chevalier RA. ApJ. 1996; 461:993.

Fraser M, et al. ApJL. 2013; 779:L8.

Freedman WL, et al. ApJ. 2001; 553:47.

Gal-Yam A, et al. Natur. 2014; 509:471.

Gehrels N, et al. ApJ. 2004; 611:1005.

Heger A, Fryer CL, Woosley SE, Langer N, Hartmann DH. ApJ. 2003; 591:288.

Hopkins AM, Beacom JF. ApJ. 2006; 651:142.

Humphreys RM, Davidson K. PASP. 1994; 106:1025.

Hurley JR, Pols OR, Tout CA. MNRAS. 2000; 315:543.

Hurley JR, Tout CA, Pols OR. MNRAS. 2002; 329:897.

Immler S, et al. ApJL. 2008; 674:L85.

Ivanova N, et al. A&ARv. 2013; 21:59.

Izzard RG, Dray LM, Karakas AI, Lugaro M, Tout CA. A&A. 2006; 460:565.

Izzard RG, Glebbeek E, Stancliffe RJ, Pols OR. A&A. 2009; 508:1359.

Izzard RG, Tout CA, Karakas AI, Pols OR. MNRAS. 2004; 350:407.

Janka HT. ARNPS. 2012; 62:407.

Jones S, et al. ApJ. 2013; 772:150.

Kalberla PMW, Burton WB, Hartmann D, et al. A&A. 2005; 440:775.

Kamble A, et al. ApJ. 2014; 797:2.

Kamble A, et al. ApJ. 2016; 818:111.

Kelly PL, Kirshner RP. ApJ. 2012; 759:107.

Khan R, Adams SM, Stanek KZ, Kochanek CS, Sonneborn G. ApJL. 2015; 815:L18.

Kiewe M, et al. ApJ. 2012; 744:10.

Kim M, et al. CBET. 2014; 3777:1.

Kobulnicky HA, Fryer CL. ApJ. 2007; 670:747.

Kochanek CS. I. 2011; 743:73.

Kroupa P. MNRAS. 2001; 322:231.

Leloudas, G. IAU Symp 279, Death of Massive Stars: Supernovae and Gamma-Ray Bursts. Roming, P.Kawai, N., Pian, E., editors. Cambridge: Cambridge University Press; 2012. p. 191

Li W, et al. Natur. 2011; 480:348.

Liedahl DA, Osterheld AL, Goldstein WH. ApJL. 1995; 438:L115.

Lyman J, Bersier D, James P, et al. MNRAS. 2016; 457:328.

Madau P, Pozzetti L, Dickinson M. ApJ. 1998; 498:106.

Maeda K, et al. ApJ. 2015; 807:35.

Margutti R, et al. ApJ. 2012; 751:134.

Margutti R, et al. ApJ. 2014a; 780:21.

Margutti R, et al. ApJ. 2014b; 797:107.

Margutti R, et al. ApJ. 2015; 805:159.

Marshall JR, van Loon JT, Matsuura M, et al. MNRAS. 2004; 355:1348.

Massey P, Neugent KF, Morrell N. ApJ. 2015; 807:81.

Matzner CD, McKee CF. ApJ. 1999; 510:379.

Mauerhan J, et al. MNRAS. 2014; 442:1166.

Mauerhan JC, et al. MNRAS. 2013a; 430:1801.

Mauerhan JC, et al. MNRAS. 2013b; 431:2599.

Mauron N, Josselin E. A&A. 2011; 526:A156.

Mcley L, Soker N. MNRAS. 2014; 445:2492.

Meakin, CA. PhD thesis. Univ Arizona; 2006.

Metzger BD. MNRAS. 2010; 409:284.

Mewe R, Gronenschild EHBM, van den Oord GHJ. A&AS. 1985; 62:197.

Mewe R, Lemen JR, van den Oord GHJ. A&AS. 1986; 65:511.

Milisavljevic D, Fesen RA, Leibundgut B, Kirshner RP. ApJ. 2008; 684:1170.

Milisavljevic D, et al. ApJ. 2015; 815:120.

Miller AA, Smith N, Li W, et al. AJ. 2010; 139:2218.

Modjaz, M. IAU Symp 279 Death of Massive Stars: Supernovae and Gamma-Ray Bursts. Roming, P.Kawai, N., Pian, E., editors. Cambridge: Cambridge University Press; 2012. p. 207

Modjaz M, Kewley L, Bloom JS, et al. ApJL. 2011; 731:L4.

Moffat, AFJ. Clumping in Hot-Star Winds. Hamann, W-R.Feldmeier, A., Oskinova, LM., editors. 2008. p. 17

Nakar E. ApJ. 2015; 807:172.

Ofek EO, et al. Natur. 2013; 494:65.

Ofek EO, et al. ApJ. 2014; 789:104.

Pastorello A, et al. Natur. 2007; 447:829.

Pastorello A, et al. ApJ. 2013; 767:1.

Pastorello A, et al. MNRAS. 2015; 449:1921.

Piro AL, Nakar E. ApJ. 2013; 769:67.

Piro AL, Nakar E. ApJ. 2014; 784:85.

Podsiadlowski P, Joss PC, Hsu JJL. ApJ. 1992; 391:246.

Pols OR, Schröder KP, Hurley JR, Tout CA, Eggleton PP. MNRAS. 1998; 298:525.

Prieto JL, Brimacombe J, Drake AJ, Howerton S. ApJL. 2013; 763:L27.

Quataert E, Shiode J. MNRAS. 2012; 423:L92.

Ramirez-Ruiz E, Dray LM, Madau P, Tout CA. MNRAS. 2001; 327:829.

Romano P, Guidorzi C, Segreto A, Ducci L, Vercellone S. A&A. 2014; 572:A97.

Roming PWA, et al. SSRv. 2005; 120:95.

Roming PWA, et al. ApJ. 2012; 751:92.

Rupen MP, van Gorkom JH, Knapp GR, Gunn JE, Schneider DP. AJ. 1987; 94:61.

Salas P, Bauer FE, Stockdale C, Prieto JL. MNRAS. 2013; 428:1207.

Sana H, et al. Sci. 2012; 337:444.

Sanders NE, et al. ApJ. 2012; 758:132.

Schinzel FK, Taylor GB, Stockdale CJ, Granot J, Ramirez-Ruiz E. ApJ. 2009; 691:1380.

Schlafly EF, Finkbeiner DP. ApJ. 2011; 737:103.

Schneider FRN, Izzard RG, Langer N, de Mink SE. ApJ. 2015; 805:20.

Shiode, JH. PhD thesis. Univ California; 2013.

Shiode JH, Quataert E. ApJ. 2014; 780:96.

Shiode JH, Quataert E, Cantiello M, Bildsten L. MNRAS. 2013; 430:1736.

Silverman JM, et al. ApJS. 2013; 207:3.

Smith N. ARA&A. 2014; 52:487.

Smith N, Arnett WD. ApJ. 2014; 785:82.

Smith N, Chornock R, Silverman JM, Filippenko AV, Foley RJ. ApJ. 2010a; 709:856.

Smith N, Li W, Filippenko AV, Chornock R. MNRAS. 2011; 412:1522.

Smith N, Mauerhan JC, Prieto JL. MNRAS. 2014; 438:1191.

Smith N, Mauerhan JC, Silverman JM, et al. MNRAS. 2012; 426:1905.

Smith N, Owocki SP. ApJL. 2006; 645:L45.

Smith N, et al. ApJ. 2008; 686:485.

Smith N, et al. AJ. 2010b; 139:1451.

Soderberg, A. PhD thesis. California Institute of Technology; 2007.

Soderberg AM, Nakar E, Berger E, Kulkarni SR. ApJ. 2006; 638:930.

Soderberg AM, et al. Natur. 2010; 463:513.

Soker N. MNRAS. 2013; 431:1541.

Soker N. ApJ. 2015; 800:114.

Sonneborn G, et al. ApJL. 1998; 492:L139.

Spitzer, L. Physics of Fully Ionized Gases. 2nd. New York: Interscience; 1962.

Strotjohann NL, et al. ApJ. 2015; 811:117.

Svirski G, Nakar E. ApJL. 2014; 788:L14.

Taddia F, et al. A&A. 2015; 580:A131.

Tinyanont S, et al. ApJ. 2016; 833:231.

Valenti S, et al. MNRAS. 2008; 383:1485.

van Loon JT, Cioni MRL, Zijlstra AA, Loup C. A&A. 2005; 438:273.

Wellons S, Soderberg AM, Chevalier RA. ApJ. 2012; 752:17.

Wheeler JC, Johnson V, Clocchiatti A. MNRAS. 2015; 450:1295.

Woosley SE, Heger A. ApJ. 2015; 810:34.

Woosley, SE., Weaver, TA., Taam, RE. Texas Workshop on Type I Supernovae. Wheeler, JC., editor. Austin, TX: Univ. of Texas; 1980. p. 96

Yan L, et al. ApJ. 2015; 814:108.

Yoon SC, Cantiello M. ApJL. 2010; 717:L62.
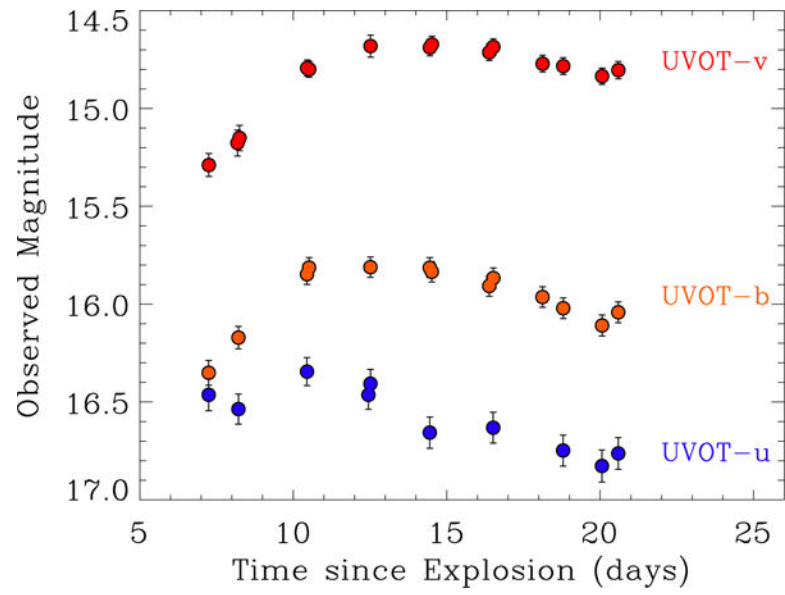
Figure 1.
Temporal evolution of SN 2014C in *u*, *b*, and *v* band as captured by *Swift*-UVOT. No host subtraction and extinction correction have been applied.
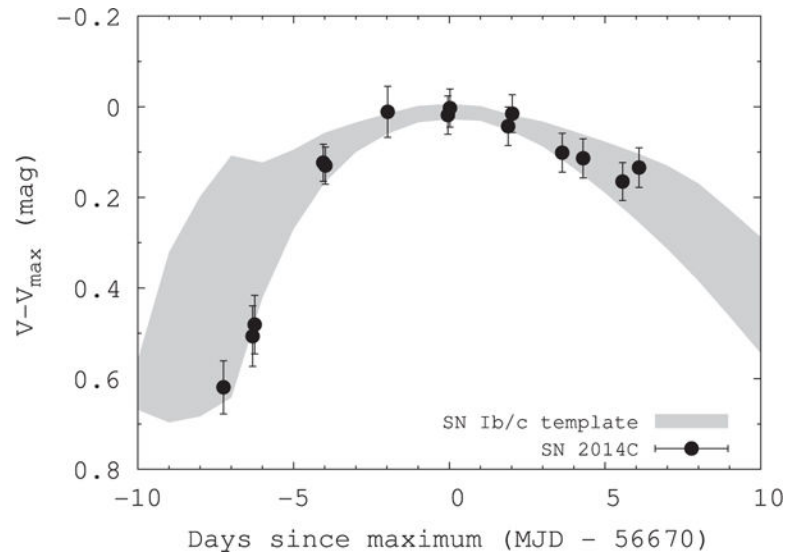
Figure 2.
Temporal evolution of the *v*-band emission from SN 2014C as observed by *Swift*-UVOT, compared to the SNe Ib/c template from Drout et al. (2011). The width of the gray curve is derived from the 1σ deviation from the mean at each epoch.
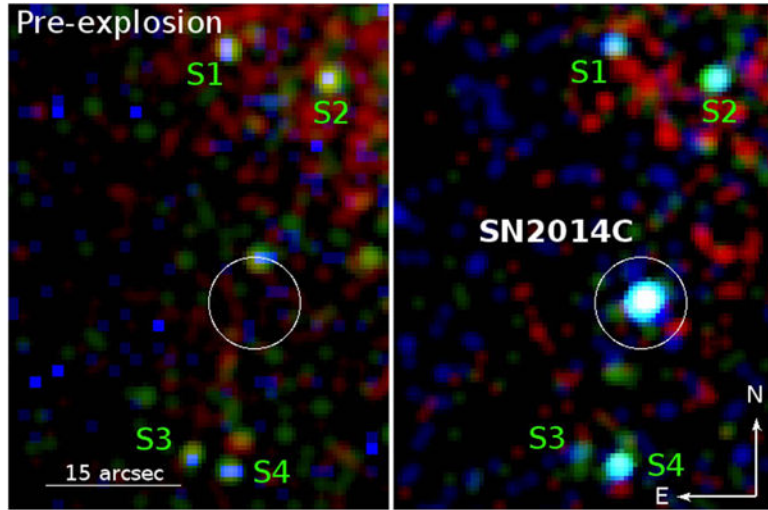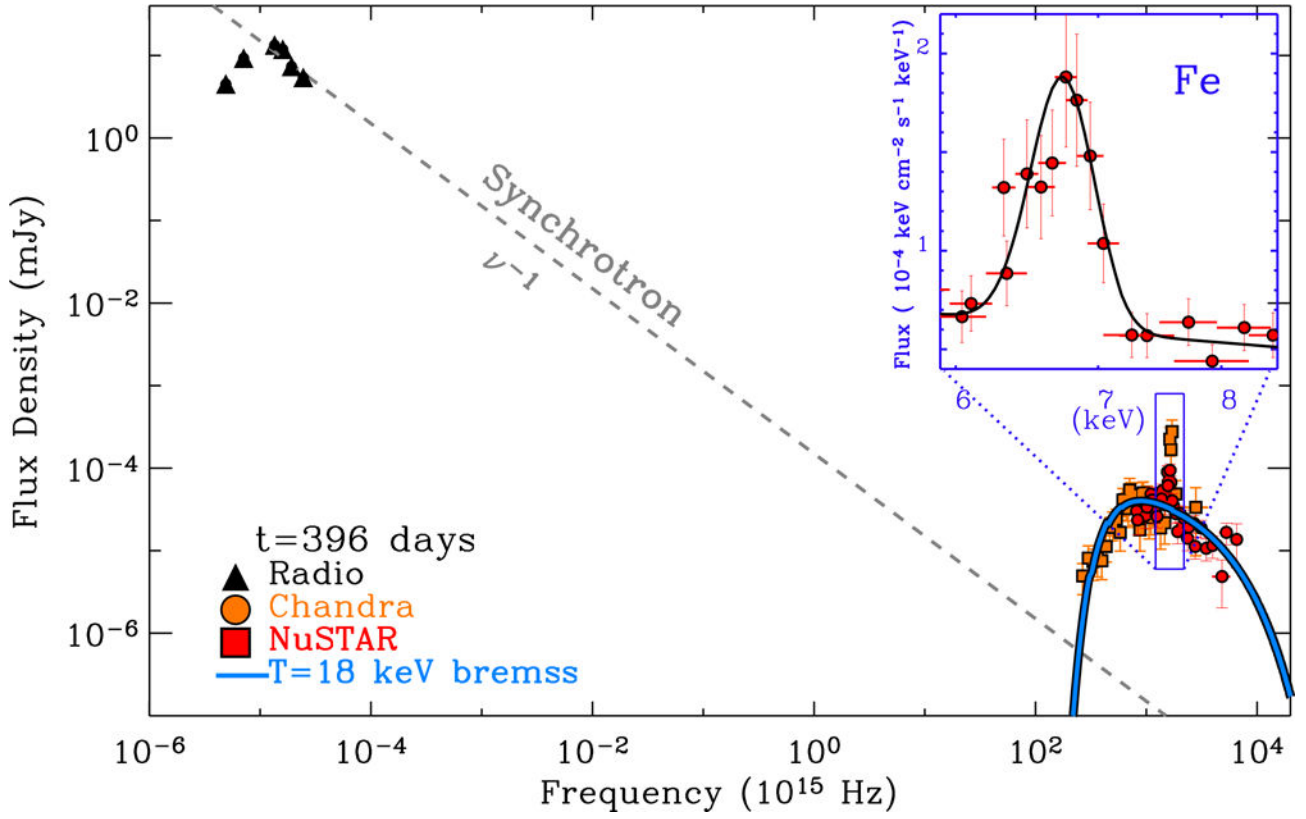
Figure 3.
Pre-and post-explosion, false-color composite X-ray images at the location of SN 2014C taken with *Chandra*. Red is for the 0.3–1 keV energy band, green for 1–3 keV photons while blue-to-white shades mark the hardest photons in the images with energy 3–10 keV. The pre-explosion image collects 29.5 ks of observations acquired in 2001. The right panel collects the post-explosion *Chandra* data presented in this paper (exposure time of 29.7 ks), covering the time period 2011 November–2015 April. SN 2014C is well detected in this time period as a bright source of hard X-ray emission. White circle: 5″ radius at the position of SN 2014C.
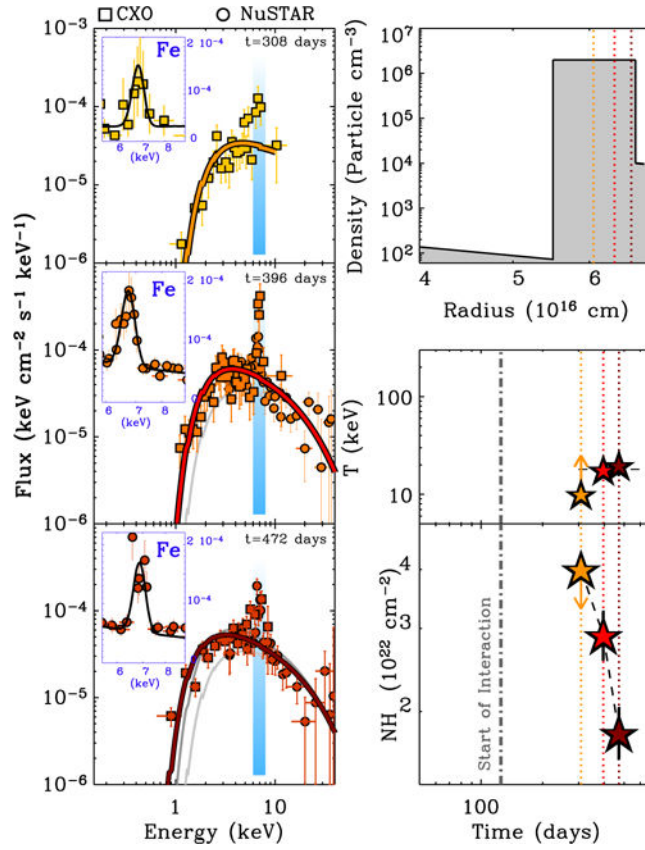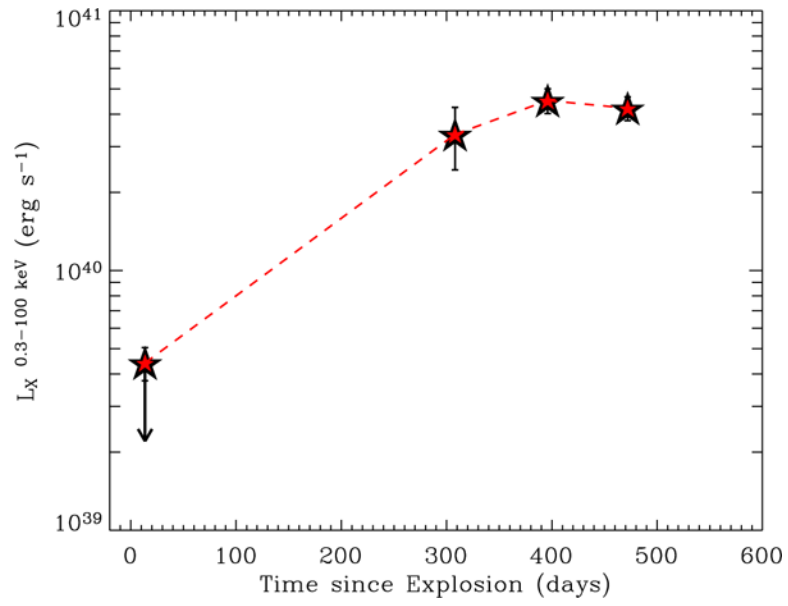
Figure 4.
Coordinated *CXO* (squares) and *NuSTAR* (filled dots) observations of SN 2014C revealed an X-ray thermally emitting plasma with characteristic temperature $T \sim 20$ keV and an absorption decreasing with time (middle and bottom panels on the right). The best-fitting bremsstrahlung model is represented with a thick colored line in each panel on the left and reproduced with gray lines in the other panels for comparison. An excess of emission around 6.7–6.9 keV is clearly detected at all epochs. We associate this emission with He-like and H-like Fe transitions. The upper right panel potrays the density profile of the environment as constrained by these observations and our modeling in Section 4.
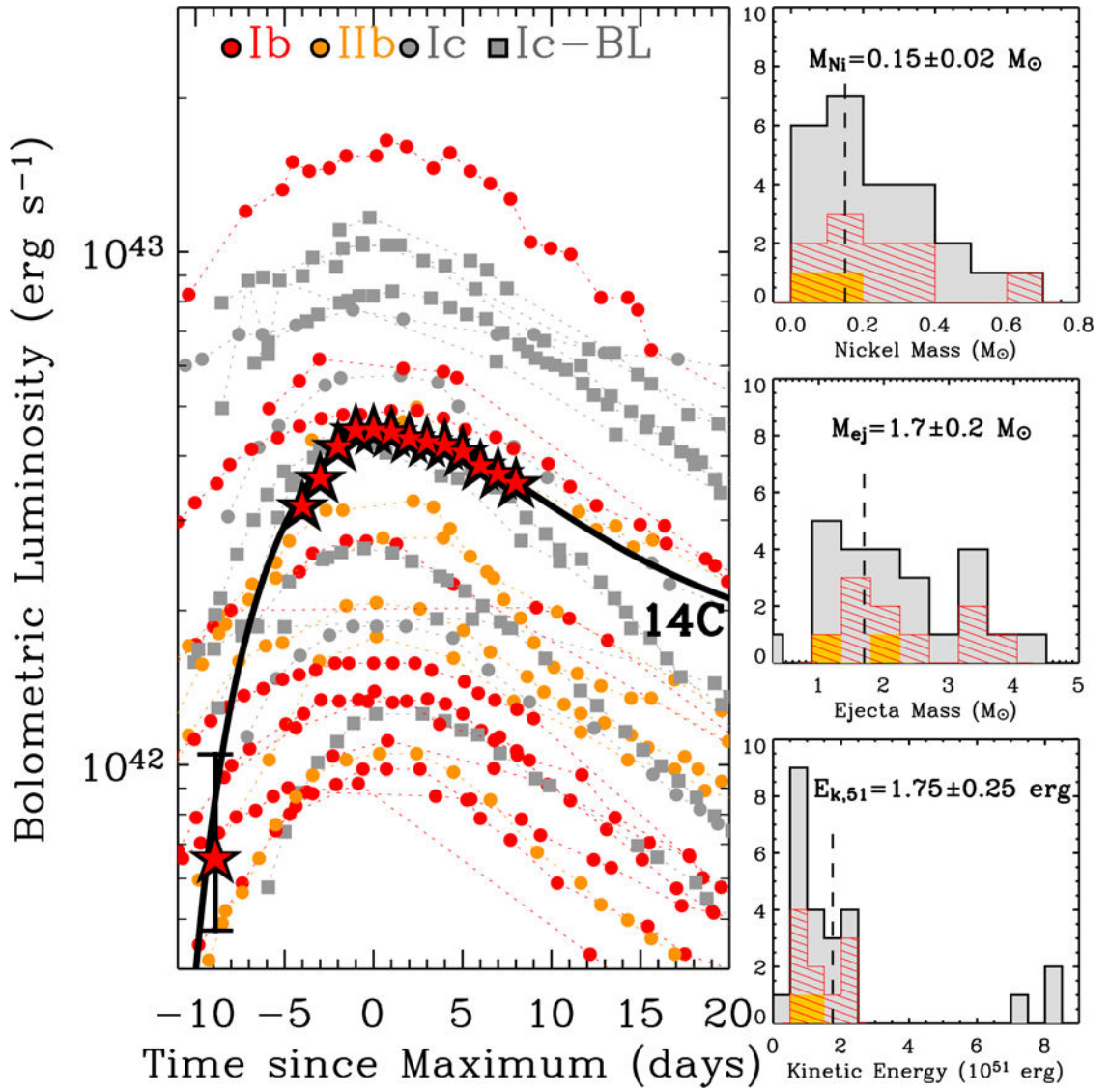
Figure 5.
Radio (VLA from K17) to hard X-ray (*CXO, NuSTAR*) spectral energy distribution of SN 2014C at $t = 396$ days after the explosion, shown here as an example. The X-ray emission is in clear excess to the synchrotron model that best fits the radio observations, as expected in the case of SN shock interaction with a very dense medium (e.g., Chevalier & Fransson 2006). *CXO* and *NuSTAR* data are best fit by an absorbed bremsstrahlung model with $T \sim$ 18 keV and $NH_{tot} \sim 3 \times 10^{22}$ cm^{-2}. Emission at 6.7–6.9 keV due to H-like and He-like Fe transitions is also clearly detected (*Inset*).
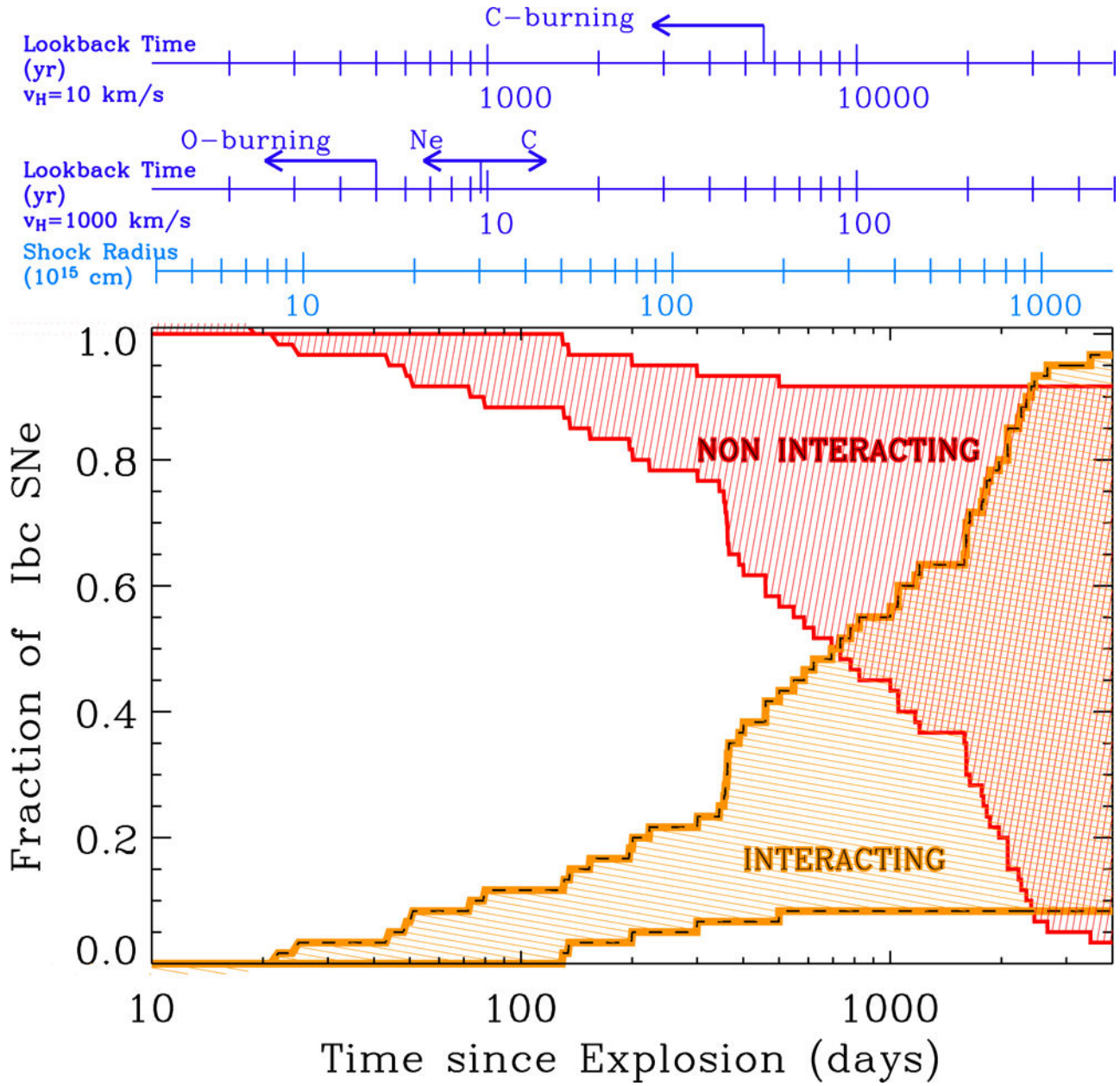
Figure 6.
Broadband X-ray light curve of SN 2014C during the first 500 days as captured by *Swift*, the *CXO* and *NuSTAR*.
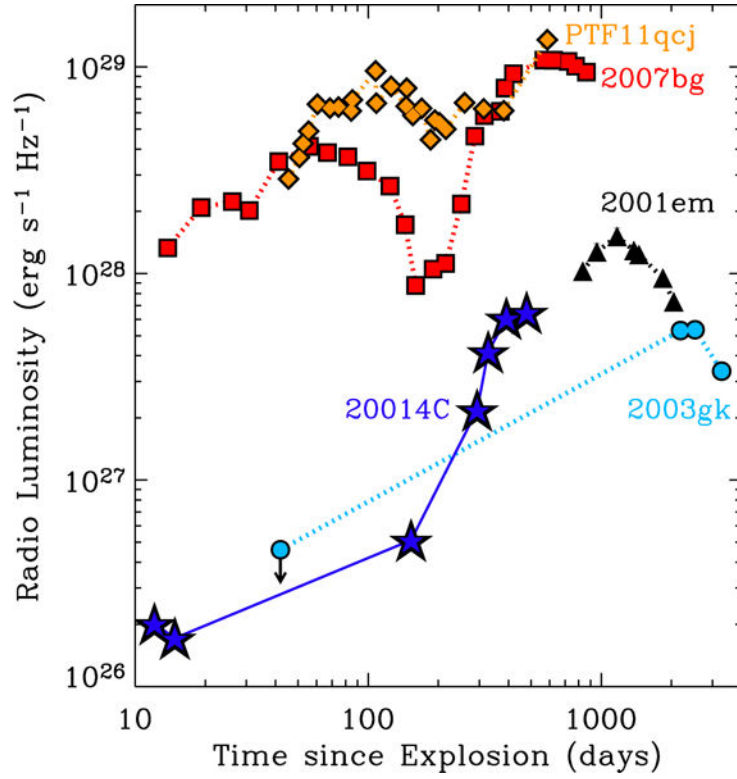
Figure 7.
Left panel: bolometric luminosity (stars) and best-fitting model (thick black line) of SN 2014C in the context of well-monitored H-poor core-collapse SNe (i.e., type Ic and Ic-BL in gray, Ib in red, and IIb in orange). Data for the other SNe are from Cano (2013), Cano & Jakobsson (2014), Cano et al. (2014), and Lyman et al. (2014). Right panels: explosion parameters of SN 2014C (vertical dashed lines) compared to the sample of Drout et al. (2011). SN 2014C shows normal explosion parameters.
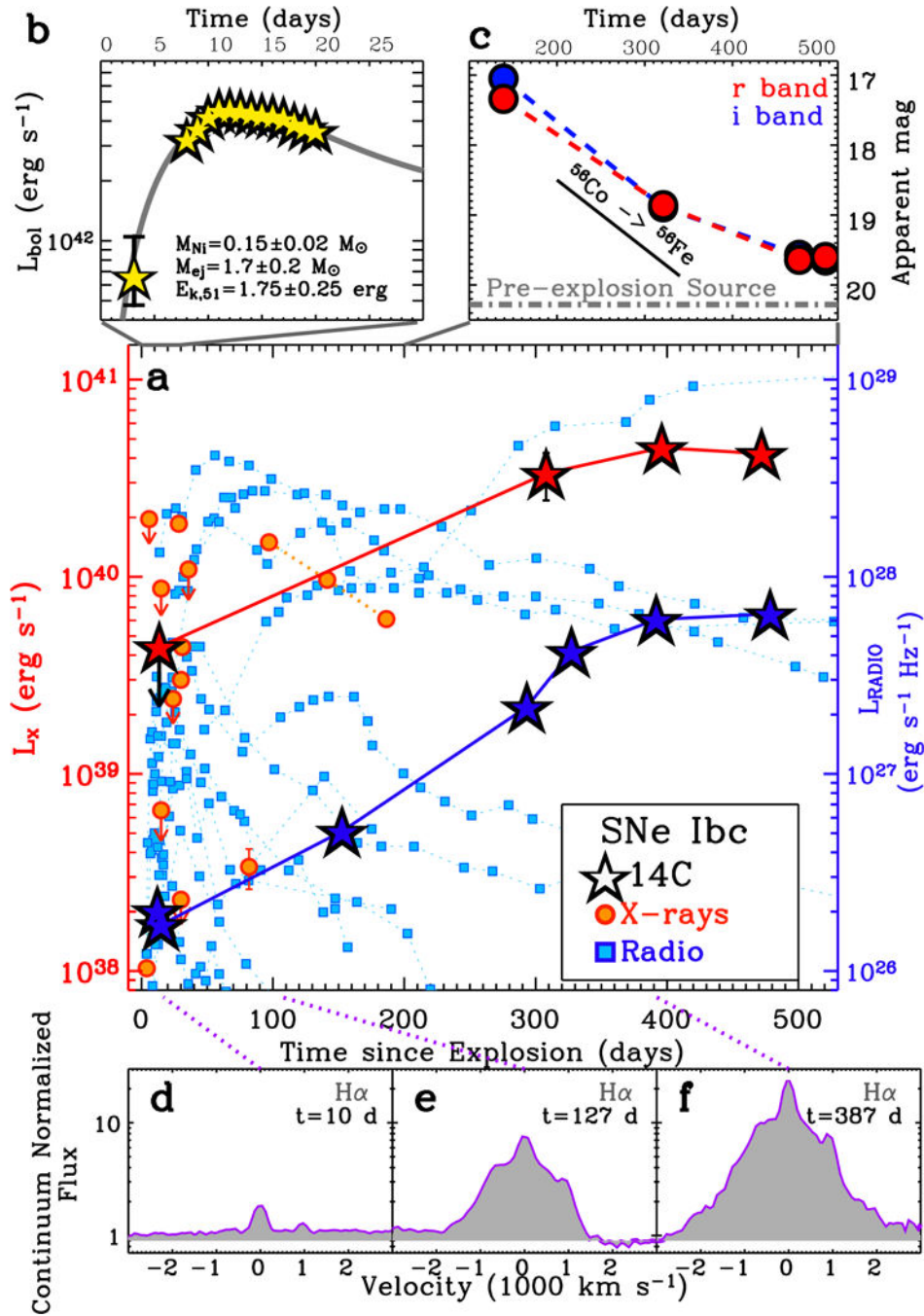
Figure 8.
Constraints on the fraction of Ib/c SNe that are interacting (orange shaded area) or non-interacting (red shaded area) with a 14C-like medium as a function of time since the explosion, as derived from the analysis of 60 SNe of type Ib/c with constraining radio observations. The fraction of objects that does not show signs of interaction at very early times is 100% by definition, as we selected spectroscopically classified type Ib/c SNe (SNe with signs of interaction since the very first moment would be instead classified as IIn or Ibn events depending on the H-rich or He-rich composition of the medium, respectively) The time since the explosion is converted into a shock radius by employing a standard shock velocity of $0.15c$. We show the lookback time for two representative ejection velocities of

the H-rich material v_H. The corresponding nuclear burning stages are for a non-rotating stellar progenitor of 12 $M_\odot$ with solar metallicity from Shiode & Quataert (2014).

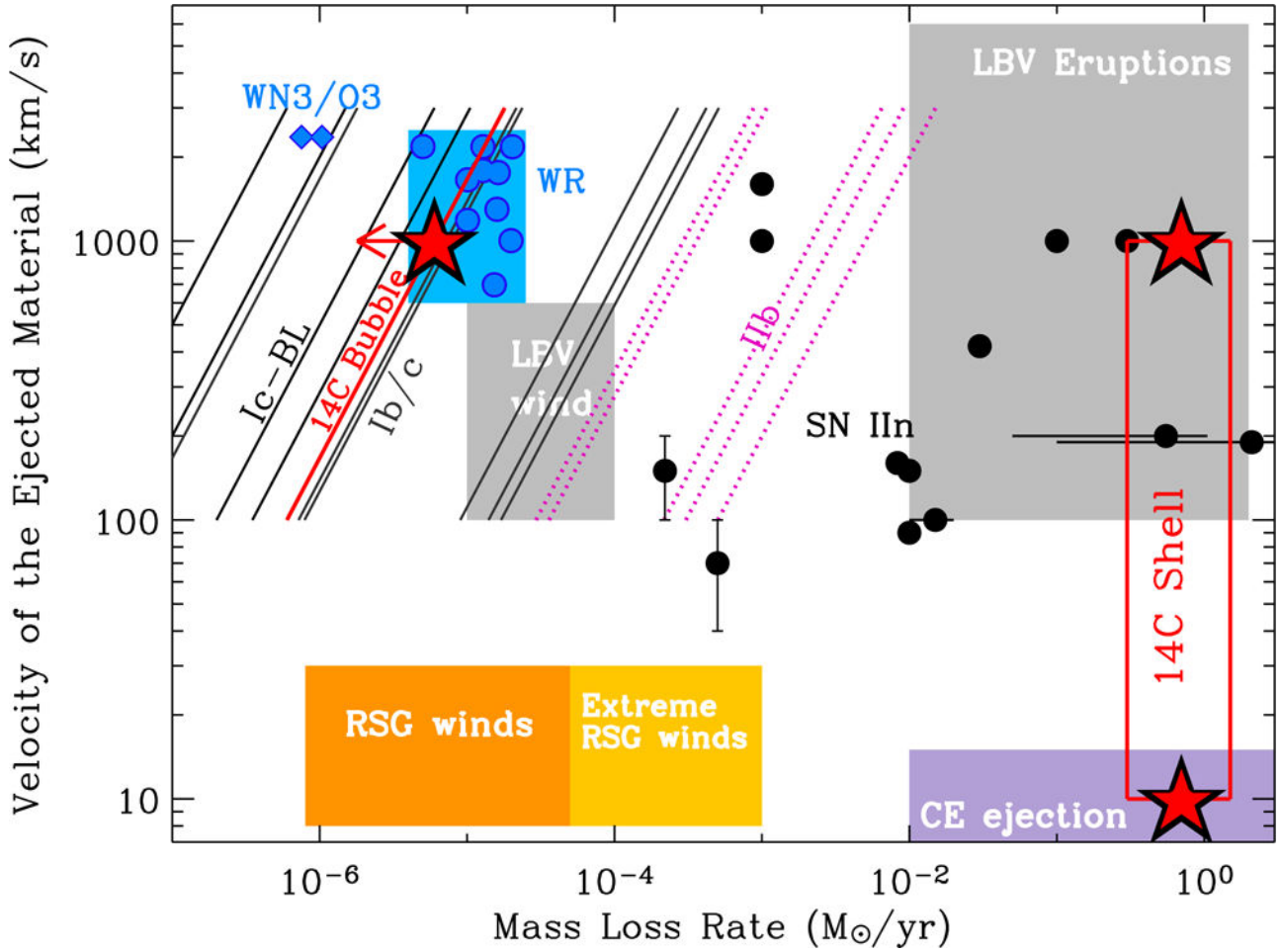**Figure 9.**
Type Ib/c SNe 2001em, 2003gk, 2007bg, and PTF11qcj display late-time radio re-brightenings with similarities to SN 2014C. 8.5 GHz data have been shown for SNe 2001em, 2003gk, and 2007bg (Schinzel et al. 2009; Salas et al. 2013; Bietenholz et al. 2014). For PTF11qcj, we show here the 7.4 GHz data from Corsi et al. (2014). For SN 2014C, we use observations acquired at 7.1 GHz (K17).

Figure 10.

This plot summarizes the key observational features of SN 2014C across the spectrum. Central panel: X-ray (red stars) and radio (7.1 GHz, blue stars) evolution of SN 2014C compared to a sample of Ib/c SNe from Margutti et al. (2014b) and Soderberg et al. (2010). SN 2014C shows an uncommon, steady increase in X-ray and radio luminosities until late times, a signature of continued shock interaction with dense CSM. Upper panels: the optical bolometric luminosity of SN 2014C is well explained at early times by a model where the source of energy is purely provided by the radioactive decay of ^{56}Ni (gray thick line, top left

panel). However, at later times (top right panel), SN 2014C shows a significantly flatter temporal decay, due to the contribution of a more efficient conversion of shock kinetic energy into radiation. This evolution is accompanied by a marked increase of Hα emission (lower panels), as a consequence of the SN shock interaction with H-rich material. See M15 and K17 for details about the spectroscopical metamorphosis and the radio evolution, respectively.

Figure 11.
Environment sampled by the SN 2014C shock evolves from the typical low-density environment around Ib/c SNe and WR stars, to the dense and rich environment typical of SNe that develop signatures of strong interaction with the medium (i.e., type-IIn SNe, here represented with black dots, data from Kiewe et al. 2012). H-poor SNe are represented with diagonal lines since the observations constrain the density ρ, which is $\propto \dot{M}/v_w$. Black, blue, and dotted purple lines are used for the sample of type Ic-BL, Ib/c, and IIb SNe from Drout et al. (2015). The properties of galactic WR stars are from Crowther (2007), while WN3/O3 stars are from Massey et al. (2015). Locations of red supergiants environments (RSG) are from de Jager et al. (1988), Marshall et al. (2004), and van Loon et al. (2005), while the typical locations of Luminous Blue Variable (LBV) winds and eruptions are inferred from Smith (2014) and Smith & Owocki (2006). For the common envelope (CE) ejection due to binary interaction, we use here a typical timescale of 1 year.

Table 1

Broadband X-ray Spectral Modeling with Thermal Bremsstrahlung

Date (days)	Instrument	Temperature T (keV)	Absorption NH_{tot} (10^{22} cm^{-2})
308	*CXO*	>10	≲4
396	*CXO+NuSTAR*	$17.8^{+3.7}_{-2.8}$	$2.9^{+0.4}_{-0.3}$
472	*CXO+NuSTAR*	$19.8^{+6.3}_{-3.9}$	$1.8^{+0.2}_{-0.2}$

Table 2

Properties of the Fe line Emission Modeled with a Gaussian Profile

Date (days)	Instrument	Central Energy E (keV)	FWHM (keV)	Flux $(10^{-13}\ \mathrm{erg\ s^{-1}\ cm^{-2}})$
308	*CXO*	6.80 ± 0.20	0.55 ± 0.23	(1.30 ± 0.30)
396	*CXO+NuSTAR*	6.70 ± 0.04	0.56 ± 0.09	(1.20 ± 0.10)
472	*CXO+NuSTAR*	6.84 ± 0.05	0.59 ± 0.14	(1.20 ± 0.10)

Table 3

Swift-UVOT Photometry

Date (day)	v (mag)	Date (day)	b (mag)	Date (day)	u (mag)	Date (day)	w1 (mag)	Date (day)	w2 (mag)	Date (day)	m2 (mag)
663.25[a]	15.29(0.06)[b]	663.25	16.35(0.06)	663.25	16.46(0.08)	663.28	17.84(0.13)	663.25	>18.68	663.26	>18.93
664.18	15.18(0.07)	664.21	16.17(0.06)	664.21	16.54(0.08)	664.21	17.69(0.10)	664.21	>18.93	664.22	>19.12
664.25	15.15(0.06)	666.45	15.85(0.05)	666.45	16.34(0.07)	666.59	17.73(0.07)	960.21	>19.10	960.21	>19.03
666.45	14.79(0.04)	666.52	15.81(0.05)	668.45	16.46(0.07)	668.59	17.76(0.07)	1013.69	>19.15	...	...
666.52	14.80(0.04)	668.52	15.81(0.05)	668.52	16.41(0.07)	670.39	17.80(0.07)	...	...	...	...
668.52	14.68(0.06)	670.45	15.81(0.05)	670.45	16.66(0.08)	672.46	17.88(0.07)	...	...	...	...
670.45	14.69(0.04)	670.52	15.83(0.05)	672.52	16.63(0.08)	674.73	18.00(0.08)	...	...	...	...
670.52	14.67(0.04)	672.39	15.91(0.05)	674.79	16.75(0.08)	676.32	17.94(0.07)	...	...	...	...
672.39	14.71(0.04)	672.52	15.87(0.05)	676.06	16.83(0.08)	960.21	>18.27	...	...	...	...
672.52	14.69(0.04)	674.12	15.96(0.05)	676.59	16.76(0.08)	...	...	...	...	...	...
674.12	14.77(0.04)	674.80	16.02(0.05)	1044.80	>17.25	...	...	...	...	...	...
674.80	14.78(0.04)	676.06	16.11(0.05)	...	...	...	...	...	...	...	...
676.06	14.83(0.04)	676.59	16.04(0.05)	...	...	...	...	...	...	...	...
676.59	14.80(0.04)	...	...	...	...	...	...	...	...	...	...

Notes.

[a] Dates are in MJD-56000 (days).

[b] Not host subtracted. Not extinction corrected. Uncertainties are 1σ.

Table 4

MMTCam Photometry

Date	*r*	*i*
795[a]	17.34(0.01)[b]	17.05(0.02)
977	18.86(0.05)	18.89(0.08)
1132	19.64(0.09)	19.57(0.13)
1162	19.60(0.09)	19.65(0.14)
1165	19.50(0.11)	19.53(0.14)

Notes.

[a]Dates are in MJD-56000 (days).

[b]Not host subtracted. Not extinction corrected. Uncertainties are 1σ.